J. Fluid Mech. (2008), *vol.* 609, *pp.* 1–48. © 2008 Cambridge University Press
doi:10.1017/S0022112008002279 Printed in the United Kingdom

Linear perturbation response of self-similar ablative flows relevant to inertial confinement fusion

J.-M. CLARISSE, C. BOUDESOCQUE-DUBOIS AND S. GAUTHIER
CEA, DIF, F-91297 Arpajon, France

(Received 20 July 2007 and in revised form 24 April 2008)

A family of exact similarity solutions for inviscid compressible ablative flows in slab symmetry with nonlinear heat conduction is proposed for studying unsteadiness and compressibility effects on the hydrodynamic stability of ablation fronts relevant to inertial confinement fusion. Dynamical multi-domain Chebyshev spectral methods are employed for computing both the similarity solution and its time-dependent linear perturbations. This approach has been exploited to analyse the linear stability properties of two self-similar ablative configurations subjected to direct laser illumination asymmetries. Linear perturbation temporal and reduced responses are analysed, evidencing a maximum instability for illumination asymmetries of zero transverse wavenumber as well as three distinct regimes of ablation-front distortion evolution, and emphasizing the importance of the mean flow unsteadiness, compressibility and stratification.

1. Introduction

When a semi-infinite initially cold material is suddenly exposed to an external heat source, a supersonic heat wave first propagates into the undisturbed material (Zel'dovich & Raizer 1967, vol. 2, chap. 10, § 8). As the heated material expands and its mass increases, the wave slows down while the sound velocity of the heated fluid increases. Owing to the increasing pressure behind the wave front, a shock wave forms which at some point overruns the heat wave. The resulting configuration of a fore-running shock wave followed by a heat front coinciding with the leading edge of an expansion wave is referred to as a heat wave in the 'deflagration regime' (Sanmartín & Barrero 1978*a*) or 'ablative heat wave' (Pakula & Sigel 1985).

Ablative heat waves are central to laser-driven inertial confinement fusion (ICF) where thermonuclear burn is expected to be achieved for a sufficiently symmetric implosion of a spherical fuel pellet (e.g. see Nuckolls *et al.* 1972; Brueckner & Jorna 1974). Such pellets are typically made of a dense shell surrounding a lighter fuel core. Their implosions under intense laser-created irradiation proceed in three stages. The 'early shell-irradiation' stage sees an ablative heat wave penetrating the outer part of the dense shell until the fore-running shock wave interacts with the shell – fuel core interface. During the subsequent 'shell acceleration' stage, the diverging rarefaction wave issued from this interaction, and the sustained shell ablation set into an inwardly accelerated motion the unablated part of the shell. In the third stage, the increasing pressure of the compressed fuel core gradually decelerates the denser outer part of the pellet until the start of thermonuclear reactions.

The hydrodynamic instability of the shell ablative heat wave front – or ‘ablation front’ – has been recognized early on as one of the key issues in the success of ICF (Nuckolls *et al.* 1972; Brueckner & Jorna 1974) as it may lead to implosion non-uniformities and possibly shell disruption, thus preventing the achievement of thermonuclear reaction conditions. Works devoted to this problem have mostly focused on the stability of strongly accelerated ablation fronts – i.e. for which the Froude number based on the front acceleration, front scale length and relative fluid velocity is small – as observed during the shell acceleration stage. The corresponding front instability – termed ‘ablative Rayleigh–Taylor’ instability owing to its acquaintance with the Rayleigh–Taylor’ instability (Rayleigh 1883; Taylor 1950) – has been the subject of numerous studies, carried out for idealized ablation flows – i.e. considering a steady ablative flow of an unbounded fluid in a uniform and constant inertial force field. Hence analytical models of the instability of discontinuous ablation fronts have been proposed for incompressible (Bodner 1974) or low-Mach-number (Kull & Anisimov 1986; Piriz, Sanz & Ibañez 1997; Piriz 2001*a*) ablation flows. Smooth ablation layer profiles have also been considered under the low-Mach-number flow approximation of Kull & Anisimov (1986), leading to most of the works in the field (Kull 1989; Bychkov *et al.* 1991, 1994; Betti *et al.* 1995, 1996), or by means of more consistent approaches (Takabe *et al.* 1985; Sanz 1996), although all restricted to subsonic ablation fronts. Analysing compressibility effects has turned out to be more arduous and has so far consisted in evaluating the influence of a finite-Mach-number expansion flow using a discontinuous ablation front model (Piriz 2001*b*). Other important features of ICF ablative flows such as unsteadiness, non-uniformity and confinement, owing to the additional complexity they introduce, have traditionally been investigated by means of multidimensional numerical simulations carried out with multiple-physics hydrodynamics codes. However, these simulations, although incorporating all of the most relevant physical phenomena, suffer from the flaws of the overly dissipative and dispersive numerical schemes used in such codes.

Similarity solutions (e.g. see Zel’dovich & Raizer 1967; Landau & Lifshitz 1987), in addition to providing insights into complex hydrodynamic phenomena, through scaling relationships, and enabling qualitative and parametric studies in realistic configurations, have been profitably used in fluid mechanics as background states for performing hydrodynamic stability analyses beyond the assumptions of uniform or steady mean flows. Self-similar ablative heat waves have been known since Marshak (1958) and have been investigated by several authors in the context of ICF (Anisimov (1970); Brun *et al.* 1977; Barrero & Sanmartín 1977; Sanmartín & Barrero 1978*a*, *b*; Reinicke & Meyer-ter-Vehn 1991; Sanz, Piriz & Tomasel 1992). Among the various configurations which have been studied, a particular family is most relevant for depicting the ablative heat wave during the early shell-irradiation stage (see Brun *et al.* 1977) for which numerical simulations indicate that mean flow profiles are more akin to self-similar than to steady flows (Velikovich *et al.* 1998). Hence such solutions present a genuine interest when investigating the stability of ablative heat waves found in ICF, including all the relevant effects of unsteadiness, compressibility and stratification. However, fully exploiting these solutions requires being able to describe both the self-similar mean flow and its perturbations in a physically consistent manner – i.e. by rendering convective and diffusive phenomena of disparate and varying scales. Part of the difficulty lies in the self-similar mean flows for which no analytical solutions are known. Hence, despite these similarity solutions being known for over four decades, their computation, at a level of accuracy compatible with a stability analysis, has been demonstrated only very recently (Boudesocque-Dubois

2000; Boudesocque-Dubois *et al.* 2001; Gauthier *et al.* 2005; Clarisse *et al.* 2006). In effect, the simplified setting of the mean flow similarity has allowed the devising of dynamical multidomain Chebyshev spectral methods for computing, respectively, the mean flow (Gauthier *et al.* 2005) and its three-dimensional time-dependent linear perturbations (Boudesocque-Dubois *et al.* 2003). Such a general and highly accurate approach opens the way to temporal stability analyses, with unprecedented details and accuracy, of a wide range of ICF ablative flows (see Boudesocque-Dubois *et al.* 2008).

As a first application, the linear responses to laser illumination asymmetries – or 'laser imprinting' – of two particular self-similar mean flows that should be achievable with the future *Laser Mégajoule* laser facility (Holstein *et al.* 2000), have been investigated (see Abéguilé *et al.* 2006). Our investigation aims at accurately rendering and identifying the role played by unsteadiness, stratification and compressibility in the early shell-irradiation ablative flow stability. This study follows a significant number of investigations of laser imprinting which have been carried out over more than a decade by means of numerical simulations, modelling or experiments.

When considering the direct illumination of an ICF pellet by laser beams, illumination asymmetries such as caused by beam non-uniformities, mispointing or imbalance, may be detrimental to the achievement of high fusion yields (e.g. Brueckner & Jorna 1974). Such asymmetries induce, during the early stage of irradiation, an ablation flow non-uniformity which will be amplified during the subsequent shell-acceleration stage, leading eventually to shell disruption and pellet performance degradation. In one of the early works on the subject, Emery *et al.* (1991) studied the impact of a laser smoothing technique on the level of flow non-uniformities by means of two-dimensional simulations. In particular, flow perturbations within the linear approximation regime were shown to induce a roughly linear time growth of areal mass perturbations while the dominance of the perturbed fore-running shock wave was emphasized.

Ishizaki & Nishihara (1997) were the first to propose an analytical model of laser imprinting by solving a linear wave equation for the supposedly uniform and adiabatic flow between the leading shock wave and the ablation front. This model which used Rankine–Hugoniot jump conditions at the shock front and Chapman–Jouguet deflagration conditions at the ablation front, reproduced the areal mass perturbation initial linear growth and subsequent saturation found in simulations (Nishihara *et al.* 1998), and gave results in agreement with experiments. Velikovich *et al.* (1998) introduced a similar model, but the ablation front boundary conditions were taken to be those of a leaky piston with exponentially time-decaying boundary pressure perturbation. The conjugated effects of the mass flux through the ablation front and of the decaying ablation front pressure perturbation were analysed as being responsible for the perturbation growth saturation which occurs for perturbation amplitudes well within the linear approximation regime. However, these simple models failed to describe the perturbation decaying oscillations observed in simulations conducted for sufficiently large times (Velikovich *et al.* 1998).

By relating these oscillations to the stabilizing mechanisms known to be at work in ablation fronts, Goncharov *et al.* (2000) went further into the modelling of laser imprinting by using the discontinuous ablation front jump conditions of Piriz *et al.* (1997) in place of the cruder ablation front boundary conditions previously used. As a result, an asymptotic regime of exponentially damped front oscillations was predicted for perturbation wavelengths smaller than the expanding heat-conducting flow region.

The succession of areal mass perturbation growth, saturation and subsequent damped oscillations found in simulations and described by this last model was later confirmed by detailed experimental results of Aglitskiy *et al.* (2002) and Metzler *et al.* (2003).

Nevertheless, neglecting the mean flow unsteadiness had been pointed out by Goncharov *et al.* (2000) as a major source of discrepancies with simulation data. For this reason, Goncharov *et al.* (2006) attempted to alleviate this defect by introducing a linear time dependence of the ablation front characteristic length which enters their model.

Overcoming the low-Mach-number assumption and the neglect of the expanding heat-conducting flow structure inherent in the discontinous ablation front model of Piriz *et al.* (1997) is also a necessity since stratification and compressibility are thought to be influential during the early shell-irradiation stage (Velikovich *et al.* 1998; Piriz & Portugues 2003). This stage which is critical to ICF pellet implosions since it sets initial conditions for the subsequent ablative Rayleigh–Taylor instability growth, requires an accurate rendering of perturbed ablative flow evolutions (see Aglitskiy *et al.* 2002; Metzler *et al.* 2003). Hence, despite improvements in the modelling of laser imprinting, substantial progress in the accurate description and analysis of this phenomenon for realistic ICF ablative flows is still required. In addition to answering this need, the present paper aims at laying the groundwork for future temporal stability analyses of ICF ablative flows beyond the sole scope of laser imprinting. Given the complexity of the self-similar mean flow, the present laser imprinting analysis of unsteady compressible ablative flows consists in a study of linear perturbation response data. After introducing (§ 2) the self-similar solution family relevant to the early shell-irradiation stage of an ICF pellet implosion, we detail (§ 3) the temporal evolution equations and boundary conditions for the linear perturbation transverse Fourier modes (§§ 3.1 and B.2.1), and exhibit a possible reduction of variables for the linear perturbations (Appendix A) leading to reduced Fourier mode equations and boundary conditions (§§ 3.2, A.3 and B.2.3). After some laser imprinting background information (§ 4.1), the chosen self-similar mean flow (§ 4.2) and perturbation (§ 4.3) configurations are detailed. Results are then given under the form of Fourier mode temporal responses (§ 4.4) which are shown to present, under certain restrictions, the characteristics of the linear perturbation variable reduction. Taking advantage of this variable reduction, temporal response results are then exploited to furnish reduced Fourier mode responses covering a wide range of the temporal and spectral variables (§ 4.5) thus allowing us to firmly establish our findings. A simple illustration of a possible practical application is also given by assessing the influence of some of the mean flow ablation parameters on laser imprinting (§ 4.6). Finally, we discuss our findings with respect to known results on the subject (§ 4.7).

2. One-dimensional self-similar ablative flows

Hydrodynamic instabilities in ICF ablative flows are classically investigated by considering the motion of an inviscid heat-conducting fluid with a polytropic equation of state,

$$p = R\rho T, \quad \mathscr{E} = C_v T \quad \text{with} \quad C_v = R/(\gamma - 1), \tag{2.1}$$

and a nonlinear heat conductivity of the form

$$\kappa = \kappa_0 \, (\rho_c/\rho)^{\mu} \, (T/T_c)^{\nu}, \quad \kappa_0 > 0, \quad \mu \geqslant 0, \quad \nu > 0, \tag{2.2}$$

where ρ, p, $\mathscr{E}$, T denote, respectively, the fluid density, pressure, specific internal energy, temperature; R is the gas constant, γ the fluid adiabatic exponent; κ_0,

μ, ν are fluid constants, and ρ_c, T_c are some reference density and temperature. Particular examples of heat conductivity exponent values are $(\mu, \nu) = (0, 5/2)$ for the Spitzer-Härm electron heat conduction model (see Duderstadt & Moses 1982) and $(\mu, \nu) = (2, 13/2)$ in the case of the radiative heat conduction for the fully ionized gas model of Kramers (see Zel'dovich & Raizer 1967). Adopting an Eulerian point of view, the equations of motion are

$$\left.\begin{aligned} &\partial_t \rho + \nabla\cdot(\rho \boldsymbol{v}) = 0, \\ &\partial_t (\rho \boldsymbol{v}) + \nabla\cdot(\rho \boldsymbol{v} \otimes \boldsymbol{v} + p\boldsymbol{I}) = \boldsymbol{0}, \\ &\partial_t[\rho(\boldsymbol{v}^2/2 + \mathscr{E})] + \nabla\cdot[\rho \boldsymbol{v}(\boldsymbol{v}^2/2 + \gamma\mathscr{E}) + \boldsymbol{\varphi}] = \mathscr{I}, \end{aligned}\right\} \tag{2.3}$$

in a Cartesian coordinate system (x, y, z), with $\boldsymbol{v}$ $(= v_x\, e_x + v_y\, e_y + v_z\, e_z)$ the fluid particle velocity, $\boldsymbol{\varphi}$ the heat flux, of expression

$$\boldsymbol{\varphi} = -\kappa \nabla T, \tag{2.4}$$

and $\mathscr{I}$ an energy source term accounting for laser energy deposition if any.

Since Marshak (1958), similarity solutions of one-dimensional forms of (2.3), or of their two-temperature counterparts in the case of plasmas, have been investigated either by means of simulations of particular initial- and boundary-value problems (IBVPs) (Anisimov 1970; Brun *et al.* 1977), either through asymptotic analysis (Barrero & Sanmartín 1977; Sanmartín & Barrero 1978*a*,*b*) or numerical integration (Reinicke & Meyer-ter-Vehn 1991) of similarity transformed equations. More recently, benefiting from an unpublished work of 1983 by Saillard (see Abéguilé *et al.* 2006), the authors and co-workers (Boudesocque-Dubois 2000; Boudesocque-Dubois *et al.* 2001; Gauthier *et al.* 2005; Abéguilé *et al.* 2006; Boudesocque-Dubois *et al.* 2008) devised a numerical approach capable of computing self-similar ablative heat waves for quasi-non-isothermal leading shock waves, with a level of accuracy compatible with a hydrodynamic stability analysis. Particular examples of such solutions for the ablation, by electron heat conduction, of semi-infinite slabs of gases in various configurations could thus be obtained (see Abéguilé *et al.* 2006; Boudesocque-Dubois *et al.* 2008).

These configurations correspond to the one-dimensional flow of a semi-infinite slab of gas – initially at rest and of uniform finite density – resulting from applying particular time-increasing pressure and heat flux laws to its external surface. Such a flow – assumed here to be along the Cartesian coordinate x-axis – is conveniently described by the equations of motion (2.3) in the absence of laser energy deposition, i.e. for $\mathscr{I} = 0$, written in terms of the Lagrangian coordinate m such that $\mathrm{d}m = \rho\, \mathrm{d}x$. With the convention that $\bar{q}$ identifies the physical quantity q relative to such a one-dimensional flow (see table 5), the relevant equations come as

$$\left.\begin{aligned} &\partial_t (1/\bar\rho) - \partial_m \bar v_x = 0, \\ &\partial_t \bar v_x + \partial_m \bar p = 0, \\ &\partial_t \left(\bar v_x{}^2/2 + \bar{\mathscr{E}}\right) + \partial_m (\bar p \bar v_x + \bar\varphi_x) = 0 \quad \text{with} \quad \bar\varphi_x = -\bar\kappa\, \bar\rho\, \partial_m \bar T, \end{aligned}\right\} \tag{2.5}$$

where all the quantities are taken along the particle trajectories $\partial_t \bar x = \bar v_x$, i.e. are functions of (m, t), while initial and boundary conditions are given by, respectively,

$$\bar\rho(m, 0) = \rho_I, \quad \bar v_x(m, 0) = 0, \quad \bar T(m, 0) = 0, \quad m \geqslant 0, \tag{2.6}$$

$$\bar p(0, t) = \bar p_e(t) = p_*(t/t_*)^{E^e_{\bar p}}, \quad \bar\varphi_x(0, t) = \bar\varphi_e(t) = \varphi_*(t/t_*)^{E^e_{\bar\varphi}}, \quad t \geqslant 0, \tag{2.7}$$

with ρ_I the fluid initial uniform density; p_*, φ_*, t_* some characteristic boundary pressure, boundary heat flux and time; and $E^e_{\bar{p}}$, $E^e_{\bar{\varphi}}$ are constants to be determined from the similarity condition.

2.1. *Dimensionless formulation*

Taking full advantage of the generality of the self-similar representation is most conveniently ensured through the use of a dimensionless formulation for the equations of motion, here given by (2.1), (2.2), (2.4), (2.5). This formulation is chosen to rely on the quantities ρ_I, R, κ_0, and t_*, given that the reference density ρ_c may be simply chosen to be ρ_I. By virtue of the Π-theorem (e.g. see Barenblatt 1979), the seven parameters (ρ_I, R, γ, κ_0, t_*, p_*, φ_*) lead us to retain the following three dimensionless numbers

$$\gamma, \quad \mathscr{B}_p = p_* t_* R/\kappa_0, \quad \mathscr{B}_\varphi = \varphi_* \sqrt{\rho_I (t_* R/\kappa_0)^3}. \tag{2.8}$$

Using the five parameters ρ_I, R, γ, κ_0, t_*, system (2.1), (2.2), (2.4), (2.5) is then rewritten in dimensionless form, with the convention that all the quantities are replaced by their dimensionless equivalents while keeping their notation unchanged. Upon denoting for any given physical quantity q, its reference value by q_c, this transformation amounts to the definitions

$$\left.\begin{array}{l} t_c = t_*, \quad \rho_c = \rho_I, \quad x_c = R^{-1/2}\,\kappa_0^{1/2}\,t_c^{1/2}\,\rho_c^{-1/2}, \\ v_c = R^{-1/2}\,\kappa_0^{1/2}\,t_c^{-1/2}\,\rho_c^{-1/2}, \quad p_c = R^{-1}\,\kappa_0\,t_c^{-1}, \\ T_c = R^{-2}\,\kappa_0\,t_c^{-1}\,\rho_c^{-1}, \quad \varphi_c = R^{-3/2}\,\kappa_0^{3/2}\,t_c^{-3/2}\,\rho_c^{-1/2}, \end{array}\right\} \tag{2.9}$$

with, in particular, the immediate consequence that the dimensionless form of the equation of state (2.1) is

$$p = \rho\, T, \quad \mathscr{E} = T/(\gamma - 1). \tag{2.10}$$

2.2. *Self-similar formulation*

The self-similar formulation of the dimensionless system derived from (2.1), (2.2), (2.4), (2.5) is achieved, for $\nu \neq 1$, upon introducing the self-similar variable

$$\xi = m t^{-\alpha}, \tag{2.11}$$

with the definition

$$\alpha = (2\nu - 1)/(2\nu - 2), \tag{2.12}$$

and the similarity laws for the dependent variables

$$\left.\begin{array}{rclrcl} \bar{\rho}(m,t) & = & \bar{G}(\xi), & \bar{v}_x(m,t) & = & t^{\alpha-1}\bar{V}(\xi), \\ \bar{T}(m,t) & = & t^{2(\alpha-1)}\bar{\Theta}(\xi), & \bar{\varphi}_x(m,t) & = & t^{3(\alpha-1)}\bar{\Phi}(\xi), \end{array}\right\} \tag{2.13}$$

see Brun *et al.* (1977), Boudesocque-Dubois *et al.* (2008) and Appendix (A). The system of partial differential equations (2.5) reduces then to a one-dimensional system of ODEs (Abéguilé *et al.* 2006), namely

$$\mathrm{d}_\xi \boldsymbol{Y} = \boldsymbol{F}(\xi, \boldsymbol{Y}), \tag{2.14}$$

for the unknown $\boldsymbol{Y} = (\bar{G}, \bar{V}, \bar{\Theta}, \bar{\Phi})^{\top}$, where the components of the function $\boldsymbol{F}$ read

$$\left.\begin{array}{l} F_1 = \bar{G}^2\, N/D, \quad F_2 = \alpha\,\xi\, N/D, \quad F_3 = -\bar{G}^{\mu-1}\,\bar{\Theta}^{-\nu}\,\bar{\Phi}, \\ F_4 = [\alpha\,\xi\, F_3 - 2(\alpha-1)\bar{\Theta}]/(\gamma-1) - \alpha\xi\,\bar{G}\bar{\Theta}\, N/D, \end{array}\right\} \tag{2.15}$$

with

$$N = (\alpha - 1)\bar{V} + \bar{G}F_3, \quad D = \alpha^2\xi^2 - \bar{G}^2\bar{\Theta}, \tag{2.16}$$

while the initial and boundary conditions (2.6) and (2.7) are, respectively, transformed into the boundary conditions

$$\bar{G} = 1, \quad \bar{V} = 0, \quad \bar{\Theta} = 0 \quad \text{as} \quad \xi \to +\infty, \tag{2.17}$$

$$\bar{P} = \bar{G}\bar{\Theta} = \mathscr{B}_p, \quad \bar{\Phi} = \mathscr{B}_\varphi \quad \text{for} \quad \xi = 0, \tag{2.18}$$

along with the time exponent expressions

$$E^e_{\bar{p}} = 2(\alpha - 1), \quad E^e_{\bar{\varphi}} = 3(\alpha - 1), \tag{2.19}$$

in (2.7). Any solution $\boldsymbol{Y}$ of (2.14) which satisfies (2.17) and (2.18) necessarily includes the singularity $D = 0$. This singularity, which corresponds to an isothermal characteristic curve, say $m/t^\alpha = \xi_s$, of the (m, t)-plane, is circumvented by introducing, as part of the solution, an isothermal shock wave at $\xi = \xi_s$. For the configurations of ablative flows in the deflagration regime presently considered, such a shock wave penetrates the cold quiescent fluid together with an infinitesimal forerunning thermal wave (e.g. see Marshak 1958). For a shock-compressed fluid region dominated by convection effects, as is the case in this paper, this wave combination may be considered as a non-isothermal shock bounding the disturbed fluid region (Marshak 1958) – the sole approximation conceded here. Hereinafter the boundary conditions (2.17) are replaced by the Rankine–Hugoniot jump relations (B 2), at $\xi = \xi_s$, for a non-isothermal shock wave with uniform upstream state given by (2.17). These jump relations along with the boundary conditions of (2.18) hence define a nonlinear eigenvalue problem for system (2.14). In the absence of any known analytical solutions to this system, we must resort to numerical integration techniques for obtaining solutions over a wide range of the boundary condition parameters $(\mathscr{B}_p, \mathscr{B}_\varphi)$.

The numerical method we have devised (Gauthier *et al.* 2005; Boudesocque-Dubois *et al.* 2008) comprises a shooting procedure based on finite-difference schemes for obtaining a solution first guess, and a relaxation process coupled to a self-adaptive multidomain Chebyshev collocation method for computing subsequent approximations up to the desired accuracy. In practice, 9 significant digit results are commonly achieved over the domain $[0, \xi_s)$ for a 15 digit implementation of the method. Less accurate results are obtained for the boundary values at $\xi = \xi_s$ in connection with the error made upon replacing there the wave structure by a non-isothermal shock front (Boudesocque-Dubois *et al.* 2008). However, this non-isothermal bounding shock-wave approximation which evidently restrains the variety of configurations that may be handled by the present method, allows the treatment of ablative flows relevant to ICF (Abéguilé *et al.* 2006). Although the question of whether or not such similarity solutions are attractors has yet to be theoretically addressed, examples of the self-similar character of converged numerical approximations to the IBVP (2.5)–(2.7) have been shown in different instances (see Brun *et al.* 1977; Boudesocque-Dubois & Clarisse 2003; Boudesocque-Dubois *et al.* 2008).

3. Linear perturbations

In fluid mechanics, the linear stability problem of a mean flow is classically formulated in terms of perturbations which, without further assumption, are functions of three space variables and time. Here, these perturbations are sought as solutions of an IBVP given by: (*a*) a linearized form of the three-dimensional Euler equations (2.3); (*b*) linear perturbations of the boundary conditions satisfied by the mean flow under study; and (*c*) initial conditions. In the present case (Boudesocque-Dubois 2000; Boudesocque-Dubois *et al.* 2001; Abéguilé *et al.* 2006), an Eulerian description of the perturbations in the (m, y, z)-coordinate system has been retained in formulating this IBVP. This particular choice follows not only from the coordinate system used for the one-dimensional solution, but also from the fact that a Lagrangian description of the perturbations would further complicate the definition of initial conditions. Indeed, in the case of a Lagrangian description, initial position perturbations would have to be supplied in addition to the initial conditions required by an Eulerian description.

The system of equations satisfied by three-dimensional linear perturbations of solutions to (2.3) is derived in the following manner. First, the change of variables $(x, y, z) \rightarrow (m, y, z)$, with m defined as in § 2, is performed in (2.3) with the help of the partial derivative transformations

$$\partial_x \longrightarrow \bar{\rho}\, \partial_m, \quad \partial_t \longrightarrow \partial_t - \bar{\rho}\, \bar{v}_x\, \partial_m \,.$$

In this new formulation, all the flow quantities are then assumed to depend on a perturbation parameter, say ε, such that $\varepsilon = 0$ corresponds to the mean flow, i.e. $q(m, y, z, t; \varepsilon)|_{\varepsilon=0} \equiv \bar{q}(m, t)$ for any scalar quantity q. By defining the linear perturbation of q to be the partial derivative

$$q^{(1)}(m, y, z, t) = \frac{\partial q}{\partial \varepsilon}(m, y, z, t; \varepsilon)|_{\varepsilon=0} \,, \tag{3.1}$$

the equations satisfied by $\rho^{(1)}$, $\boldsymbol{v}^{(1)}$, $\mathscr{E}^{(1)}$ are obtained formally by differentiating, with respect to ε, the equations in the (m, y, z, t)-variables, considering m, y, z, t and ε to be the independent variables. This definition corresponds to an Eulerian description of the perturbations (e.g. see Ledoux & Walraven 1958, § 56) in the coordinate system (m, y, z). The resulting system of linear perturbation equations then becomes

$$\partial_t \rho^{(1)} + \bar{\rho}\left[\partial_m\left(\bar{\rho}\, v_x^{(1)}\right) + \partial_m \bar{v}_x\, \rho^{(1)} + \nabla_\perp \cdot \boldsymbol{v}_\perp^{(1)}\right] = 0, \tag{3.2a}$$

$$\partial_t v_x^{(1)} + \bar{\rho} \partial_m \bar{v}_x\, v_x^{(1)} + \partial_m p^{(1)} - \partial_m \bar{p}\, \rho^{(1)}/\bar{\rho} = 0, \tag{3.2b}$$

$$\partial_t \boldsymbol{v}_\perp^{(1)} + \nabla_\perp p^{(1)}/\bar{\rho} = \boldsymbol{0}, \tag{3.2c}$$

$$\begin{aligned} &\partial_t \mathscr{E}^{(1)} + \bar{\rho} \partial_m \bar{\mathscr{E}}\, v_x^{(1)} + \bar{\rho}\, \partial_m \bar{v}_x\, T^{(1)} + \bar{p}\, \partial_m v_x^{(1)} \\ &\quad + \partial_m \varphi_x^{(1)} - \partial_m \bar{\varphi}_x \rho^{(1)}/\bar{\rho} + \left(\bar{p} \nabla_\perp \cdot \boldsymbol{v}_\perp^{(1)} + \nabla_\perp \cdot \boldsymbol{\varphi}_\perp^{(1)}\right)/\bar{\rho} = 0, \end{aligned} \tag{3.2d}$$

where $\nabla_\perp . = (\partial_y ., \partial_z .)^\top$, and with the notation $\boldsymbol{v}_\perp^{(1)} = v_y^{(1)} \boldsymbol{e}_y + v_z^{(1)} \boldsymbol{e}_z$, $\boldsymbol{\varphi}_\perp^{(1)} = \varphi_y^{(1)} \boldsymbol{e}_y + \varphi_z^{(1)} \boldsymbol{e}_z$, for, respectively, the transverse velocity field and heat flux linear perturbations (see also table 5). These equations are supplemented by the expressions for the heat flux linear perturbations, or

$$\varphi_x^{(1)} = -\bar{\rho}\bar{\kappa}(\partial_m T^{(1)} + \partial_m \bar{T}\,[(1-\mu)\rho^{(1)}/\bar{\rho} + \nu T^{(1)}/\bar{T}]), \tag{3.3a}$$

$$\boldsymbol{\varphi}_\perp^{(1)} = -\bar{\kappa} \nabla_\perp T^{(1)}, \tag{3.3b}$$

and the linearized form of the equation of state (2.10),

$$p^{(1)} = \bar{\rho}\, T^{(1)} + \rho^{(1)}\, \bar{T}, \quad \mathscr{E}^{(1)} = T^{(1)}/(\gamma - 1). \tag{3.4}$$

The above system of linear perturbation PDEs may be simplified upon introducing a Helmholtz decomposition of the transverse velocity field $\boldsymbol{v}_\perp^{(1)}$. From this decomposition, the irrotational part of $\boldsymbol{v}_\perp^{(1)}$ is entirely determined by the transverse expansion $\nabla_\perp \cdot \boldsymbol{v}_\perp^{(1)}$, which obeys the evolution equation

$$\partial_t\left(\nabla_\perp \cdot \boldsymbol{v}_\perp^{(1)}\right) + \Delta_\perp p^{(1)}/\bar{\rho} = 0\,, \tag{3.5}$$

while the remaining – solenoidal – part of $\boldsymbol{v}_\perp^{(1)}$ is reduced to steady solid rotations about the x-axis, with angular velocities stipulated by initial conditions. This latter type of motion is of little interest in the present case and is discarded, hence leading to the three-dimensional system of PDEs (3.2*a*), (3.2*b*), (3.5), (3.2*d*) for the unknowns $(\rho^{(1)}, v_x^{(1)}, \nabla_\perp \cdot \boldsymbol{v}_\perp^{(1)}, \mathscr{E}^{(1)})$ as functions of (m, y, z, t). This system of PDEs can be shown to be incompletely parabolic in the sense of Gustafsson & Sundström (1978), Strikwerda (1977), and well-posed for the Cauchy problem: details will be published elsewhere. Consequently, at any given boundary, the proper number of independent boundary conditions to be applied is given by the number of incoming waves of the hyperbolic subsystem plus one. Note that up to this point, the formulation of (3.2*a*), (3.2*b*), (3.5), (3.2*d*) applies to any one-dimensional mean flow satisfying (2.1), (2.2), (2.4), (2.5).

When dealing with the ablative mean flows discussed in (§ 2.2), boundary conditions are provided at the shock-wave front location, $m = \xi_s\, t^\alpha$, by the Rankine–Hugoniot relations for linear perturbations (B 4). At the fluid external boundary $m = 0$ of equation $x = x_e(y, z, t; \varepsilon)$, arbitrary time-dependent perturbations of the fluid density and of the incident heat-flux are considered, so that we have

$$\rho(m, y, z, t; \varepsilon)|_+ = \rho_e(y, z, t; \varepsilon),$$
$$(\boldsymbol{\varphi}(m, y, z, t; \varepsilon)|_+ - \boldsymbol{\varphi}_e(y, z, t; \varepsilon)) \cdot \boldsymbol{n}_e = 0,$$

or, in terms of linear perturbations,

$$\rho^{(1)}\big|_+ + (\bar{\rho}\partial_m\bar{\rho})|_+\, x_e^{(1)} = \rho_e^{(1)}, \tag{3.6}$$

$$\varphi_x^{(1)}\big|_+ + (\bar{\rho}\partial_m\bar{\varphi}_x)|_+\, x_e^{(1)} = \varphi_{e_x}^{(1)}, \tag{3.7}$$

where $\boldsymbol{n}_e$ denotes the normal to the surface and $q|_+$ stands for the limiting value of the fluid quantity $q(m, y, z, t)$ as $m \to 0^+$. In these equations, the linear deformation, along the x-direction, of the fluid external perturbed surface, $x_e^{(1)}$, satisfies the well-known linearized kinematic boundary condition for a material surface (e.g. see Stoker 1958), in effect

$$\dot{x}_e^{(1)} = v_x^{(1)}\big|_+ + (\bar{\rho}\partial_m\bar{v}_x)|_+\, x_e^{(1)}. \tag{3.8}$$

3.1. *Fourier mode evolution equations*

The self-similar nature of the mean flows of § 2 naturally suggests a reformulation of the system of PDEs (3.2*a*), (3.2*b*), (3.5), (3.2*d*) and of the boundary conditions (3.6)–(3.8), (B 4) in the independent variables (ξ, y, z, t). This new formulation simply proceeds from applying (2.13) and the partial derivative transformations

$$\partial_t q^{(1)}(m, y, z, t) = \left(\partial_t - \alpha\xi t^{-1}\partial_\xi\right) Q(\xi, y, z, t),$$
$$\partial_m q^{(1)}(m, y, z, t) = t^{-\alpha}\partial_\xi\, Q(\xi, y, z, t),$$

with the convention $Q(\xi, y, z, t) \equiv q^{(1)}(m, y, z, t)$, for any flow variable linear perturbation $q^{(1)}$. Once Fourier transformed in the (y, z) variables, the ensuing equations yield a system of linear PDEs in the independent variables (ξ, t). With the definition

$$\mathfrak{F}_{yz}[q^{(1)}(m, y, z, t)] = \int_{-\infty}^{+\infty}\int_{-\infty}^{+\infty} q^{(1)}(m, y, z, t)\, \exp[-\mathrm{i}(k_y\, y + k_z\, z)]\, \mathrm{d}z\, \mathrm{d}y,$$

and the notations (see table 5)

$$\left.\begin{aligned}
\widehat{G}(\xi,k_\perp,t) &\equiv \mathfrak{F}_{yz}[\rho^{(1)}(m,y,z,t)], & \widehat{V}_x(\xi,k_\perp,t) &\equiv \mathfrak{F}_{yz}\big[v_x^{(1)}(m,y,z,t)\big],\\
\widehat{D}_\perp(\xi,k_\perp,t) &\equiv \mathfrak{F}_{yz}[\nabla_\perp\cdot\boldsymbol{v}_\perp^{(1)}(m,y,z,t)], & \widehat{\Theta}(\xi,k_\perp,t) &\equiv \mathfrak{F}_{yz}[T^{(1)}(m,y,z,t)],\\
\widehat{P}(\xi,k_\perp,t) &\equiv \mathfrak{F}_{yz}[p^{(1)}(m,y,z,t)], & \widehat{\Phi}_x(\xi,k_\perp,t) &\equiv \mathfrak{F}_{yz}\big[\varphi_x^{(1)}(m,y,z,t)\big],
\end{aligned}\right\} \tag{3.9}$$

where

$$k_\perp = \sqrt{k_y^2 + k_z^2},$$

is the modulus of the transverse wave vector $\boldsymbol{k}_\perp$, this system reads

$$\left.\begin{aligned}
\partial_t\widehat{G} &= t^{-1}(\alpha\xi\partial_\xi - \bar{G}\mathrm{d}_\xi\bar{V})\,\widehat{G} - t^{-\alpha}\bar{G}\,\partial_\xi(\bar{G}\,\widehat{V}_x) - \bar{G}\,\widehat{D}_\perp,\\
\partial_t\widehat{V}_x &= t^{-1}(\alpha\xi\partial_\xi - \bar{G}\mathrm{d}_\xi\bar{V})\,\widehat{V}_x + t^{\alpha-2}\mathrm{d}_\xi\bar{P}\,\widehat{G}/\bar{G} - t^{-\alpha}\partial_\xi\widehat{P},\\
\partial_t\widehat{D}_\perp &= t^{-1}\alpha\xi\partial_\xi\widehat{D}_\perp + k_\perp^2\,\widehat{P}/\bar{G},\\
\partial_t\widehat{\Theta} &= t^{-1}[\alpha\xi\partial_\xi - (\gamma-1)\bar{G}\mathrm{d}_\xi\bar{V}]\,\widehat{\Theta} - t^{\alpha-2}[(\gamma-1)\bar{P}\,\partial_\xi + \bar{G}\mathrm{d}_\xi\bar{\Theta}]\widehat{V}_x\\
&\quad -(\gamma-1)(t^{2\alpha-2}\bar{\Theta}\,\widehat{D}_\perp + t^{2\alpha-1}k_\perp^2\bar{G}^{-\mu-1}\bar{\Theta}^{\nu}\widehat{\Theta}\\
&\quad -t^{2\alpha-3}\mathrm{d}_\xi\bar{\Phi}\,\widehat{G}/\bar{G} + t^{-\alpha}\partial_\xi\widehat{\Phi}_x),
\end{aligned}\right\} \tag{3.10}$$

with the expressions

$$\widehat{\Phi}_x = -t^{\alpha-1}\bar{G}^{1-\mu}\bar{\Theta}^{\nu}(\partial_\xi\widehat{\Theta} + \mathrm{d}_\xi\bar{\Theta}\,[t^{2\alpha-2}(1-\mu)\widehat{G}/\bar{G} + \nu\widehat{\Theta}/\bar{\Theta}]), \tag{3.11}$$

as inferred from (3.3*a*), and

$$\widehat{P} = \bar{G}\,\widehat{\Theta} + t^{2\alpha-2}\widehat{G}\,\bar{\Theta}, \tag{3.12}$$

after (3.4). The relevant formulation of the boundary condition equations (3.6)–(3.8) also becomes

$$\widehat{G}|_+ + t^{-\alpha}(\bar{G}\mathrm{d}_\xi\bar{G})|_+\widehat{X}_e = \widehat{G}_e, \tag{3.13}$$

$$\widehat{\Phi}_x|_+ + t^{2\alpha-3}(\bar{G}\mathrm{d}_\xi\bar{\Phi})|_+\widehat{X}_e = \widehat{\Phi}_{ex}, \tag{3.14}$$

$$\dot{\widehat{X}}_e = \widehat{V}_x|_+ + t^{-1}(\bar{G}\mathrm{d}_\xi\bar{V})|_+\widehat{X}_e, \tag{3.15}$$

with the notation $\widehat{X}_e(k_\perp,t)\equiv\mathfrak{F}_{yz}[x_e^{(1)}(y,z,t)]$, while the linear perturbation Rankine–Hugoniot relations (B 4) take the form of (B 5). Since the transverse wave vector $\boldsymbol{k}_\perp$ solely intervenes in (3.10)–(3.15) through its modulus, solutions $(\widehat{G}, \widehat{V}_x, \widehat{D}_\perp, \widehat{\Theta})$ of the associated IBVPs may be considered as functions of $(\xi, k_\perp, t)$ only – solutions for different wave vectors $\boldsymbol{k}_\perp$ of identical modulus $k_\perp$ being then distinguished by their initial or boundary conditions.

System (3.10), being incompletely parabolic, is handled via an operator decomposition between a reduced hyperbolic system (Boudesocque-Dubois *et al.* 2003) and a parabolic scalar equation, along with a proper distribution of boundary conditions among these subsystems. Numerical approximation in the ξ variable is performed with the same adaptive multidomain spectral method as that used for the mean flow while time-marching is carried out with a three-step semi-implicit Runge–Kutta scheme (Williamson 1980). Treatments of time-dependent boundary conditions such as those of (3.13), (3.15), (B 5), and of matching conditions at computational subdomain interfaces for the hyperbolic subsystem are addressed by Boudesocque-Dubois *et al.* (2003) and Gauthier *et al.* (2005). Solutions of the parabolic scalar equation are computed following the influence matrix technique developed by Pulicani (1988). Arbitrary perturbed configurations of the present self-similar ablative flows may be handled with this general method. In particular, linear perturbation boundary conditions other than those defined by (3.13) and (3.14) may equally be considered.

3.2. *Reduced Fourier mode equations*

Given the self-similar nature of the mean flows of §2.2, we may wonder whether system (3.10) also admits a reduced variable formulation of some kind. This turns out to be the case under particular assumptions bearing on the linear perturbations, system (3.10) being then replaced by a reduced system of two-dimensional PDEs where the time variable has been removed (see Appendix A for details).

Such a linear perturbation variable reduction amounts to rewriting (3.2*a*), (3.2*b*), (3.2*d*), (3.5) in terms of the independent variables (ξ, η, ζ, t), with ξ given by (2.11), η and ζ by the analogous relations

$$\eta = y\,t^{-\alpha}, \quad \zeta = z\,t^{-\alpha}, \tag{3.16}$$

the exponent α keeping its definition (2.12), while assuming, in addition to the mean flow quantity dependencies (2.13), the following perturbation time power-law dependencies

$$\left.\begin{aligned}
\rho^{(1)}(m, y, z, t) &= t^{(\delta-1)(\alpha-1)}\,\mathscr{G}(\xi, \eta, \zeta),\\
T^{(1)}(m, y, z, t) &= t^{(\delta+1)(\alpha-1)}\,\mathscr{T}(\xi, \eta, \zeta),\\
v_a^{(1)}(m, y, z, t) &= t^{\delta(\alpha-1)}\,\mathscr{V}_a(\xi, \eta, \zeta), \quad a = x, y, z,\\
\varphi_a^{(1)}(m, y, z, t) &= t^{(\delta+2)(\alpha-1)}\,\mathscr{F}_a(\xi, \eta, \zeta), \quad a = x, y, z,
\end{aligned}\right\} \tag{3.17}$$

where δ is a free parameter, defined by (A 2). The resulting system of equations, once Fourier transformed in the (η, ζ) variables, ultimately leads to a system of linear PDEs in the $(\xi, \varkappa_\perp)$ variables (see §A.3) where $\varkappa_\perp = k_\perp t^\alpha$ – the 'reduced wavenumber' – is the modulus of the wave vector in the (η, ζ)-Fourier space. Upon introducing the notations (cf. also table 5)

$$\widehat{\mathscr{G}}, \quad \widehat{\mathscr{V}}_x, \quad \widehat{\mathscr{D}}_\perp, \quad \widehat{\mathscr{T}}, \quad \widehat{\mathscr{P}}, \quad \widehat{\mathscr{F}}_x,$$

for the $\eta\zeta$-Fourier transforms – or 'reduced Fourier modes' – of the linear perturbation reduced functions

$$\mathscr{G}, \quad \mathscr{V}_x, \quad \nabla_{(\eta,\zeta)} \cdot \mathscr{V}_\perp, \quad \mathscr{T}, \quad \mathscr{P}, \quad \mathscr{F}_x,$$

see (A 19), this system of reduced PDEs becomes

$$\left.\begin{aligned}
&[(\delta-1)(\alpha-1) - \alpha(\xi\partial_\xi - \mathbb{D})](\widehat{\mathscr{G}}/\bar{G}) + \partial_\xi(\bar{G}\widehat{\mathscr{V}}_x) + \widehat{\mathscr{D}}_\perp = 0,\\
&[\delta(\alpha-1) - \alpha(\xi\partial_\xi - \mathbb{D})]\widehat{\mathscr{V}}_x + \bar{G}\,\mathrm{d}_\xi \bar{V}\,\widehat{\mathscr{V}}_x + \partial_\xi\widehat{\mathscr{P}} - \mathrm{d}_\xi\bar{P}\,\widehat{\mathscr{G}}/\bar{G} = 0,\\
&[\delta(\alpha-1) - \alpha(\xi\partial_\xi - \mathbb{D})]\widehat{\mathscr{D}}_\perp - \varkappa_\perp^2\widehat{\mathscr{P}}/\bar{G} = 0,\\
&[(\delta+1)(\alpha-1) - \alpha(\xi\partial_\xi - \mathbb{D})]\widehat{\mathscr{T}} + \bar{G}\,\mathrm{d}_\xi\bar{\Theta}\,\widehat{\mathscr{V}}_x + (\gamma-1)\big(\bar{G}\,\mathrm{d}_\xi\bar{V}\,\widehat{\mathscr{T}}\\
&\quad + \bar{P}\,\partial_\xi\widehat{\mathscr{V}}_x + \partial_\xi\widehat{\mathscr{F}}_x - \mathrm{d}_\xi\bar{\Phi}\,\widehat{\mathscr{G}}/\bar{G} + \bar{\Theta}\,\widehat{\mathscr{D}}_\perp - \varkappa_\perp^2\bar{G}^{-\mu-1}\bar{\Theta}^\nu\widehat{\mathscr{T}}\big) = 0,
\end{aligned}\right\} \tag{3.18}$$

where $\mathbb{D}$ is the operator defined by (A 21). Boundary conditions (3.6)–(3.8) and (B 4) proceed similarly, yielding the ODEs (A 22) and (B 7) in the variable $\varkappa_\perp$.

An important and interesting result brought up by the possible existence of such a reduction is that for any flow variable linear perturbation $q^{(1)}$ satisfying the relation

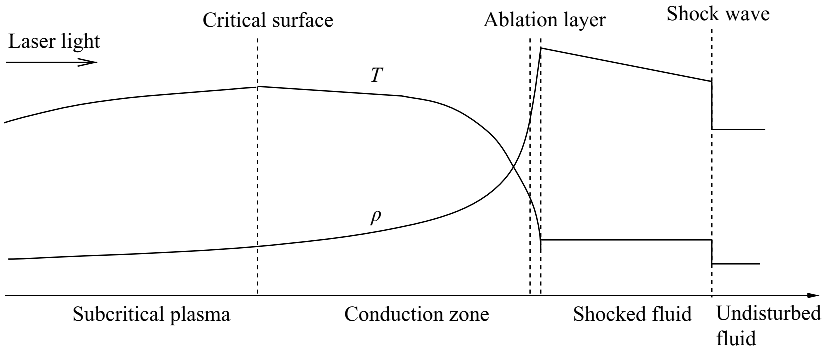

FIGURE 1. Schematic mean flow structure of an ablative heat wave under direct laser illumination in terms of density ρ and temperature T profiles.

$q^{(1)}(m, y, z, t) = t^n \mathcal{Q}(\xi, \eta, \zeta)$, its yz-Fourier transform $\widehat{Q}$ is such that

$$\widehat{Q}(\xi, k_\perp, t) \equiv \mathcal{F}_{yz}[q^{(1)}(m, y, z, t)] = t^{n+2\alpha}\, \widehat{\mathcal{Q}}(\xi, t^\alpha k_\perp). \tag{3.19}$$

Hence, although we do not actually consider, in this paper, solving boundary-value problems for system (3.18), we shall make use of this property when analysing numerical integration results of some particular IBVPs defined after (3.10).

4. Responses to laser illumination asymmetries

4.1. *Background*

The mean flow structure relevant to the early direct illumination of an ICF pellet by laser beams may be divided into five regions (cf. figure 1).

Subcritical plasma. Closest to the laser beams, the expanding laser-absorption region where the laser radiation is entirely absorbed, mostly for electron densities close to a cutoff – ‘critical’ – value determined by the laser frequency.

Conduction zone. Beyond the critical electron density plane, the supercritical part of the flow, also in expansion, which is mainly governed by electron heat conduction and where electron density is above critical.

Ablation layer. The zone of steep density and temperature gradients where energy convection becomes comparable to energy conduction.

Shocked fluid. The quasi-isentropic compression portion of the flow, up to the fore-running shock wave, where energy convection is dominant.

Undisturbed fluid. The fluid lying at rest, ahead of the shock front.

The modelling of this mean flow by the single temperature fluid equations (2.1), (2.2)–(2.4) evidently implies numerous assumptions that we shall not elaborate on at present. Comparisons of results from laser imprinting models derived from these equations and from hydrodynamics code simulations (Nishihara *et al.* 1998; Velikovich *et al.* 1998; Goncharov *et al.* 2000), and from laser imprint simulations and experiments (Taylor *et al.* 1996; Aglitskiy *et al.* 2002; Metzler *et al.* 2003) comfort these assumptions.

Several physical phenomena have been identified to play major roles in the ablation flow non-uniformity evolution.

(*a*) Laser absorption in ICF occurring close to the critical surface, the subcritical plasma may be held as nearly transparent to the incoming laser irradiation (Brueckner & Jorna 1974). Consequently, accounting for laser absorption asymmetries amounts to taking in (2.3) an energy source term $\mathscr{I}$ of compact support about the critical surface and of equivalent heat flux given by the local laser intensity.

(*b*) Temperature fluctuations forced by laser intensity asymmetries are smoothed within the conduction zone due to electron heat conduction – 'thermal smoothing' – (Brueckner & Jorna 1974; Emery *et al.* 1991) with the consequence that flow perturbations imprinted at the ablation layer by this forcing at the critical surface are increasingly damped as the perturbation wavelengths become smaller than the conduction zone thickness l_{con} (Emery *et al.* 1991).

(*c*) Each of the perturbed shock front, ablation layer and conduction zone dynamics are of importance to the ablation flow perturbation response as shown by simulations (Emery *et al.* 1991; Velikovich *et al.* 1998), modelling (Velikovich *et al.* 1998; Goncharov *et al.* 2000), and experiments (Aglitskiy *et al.* 2002).

(*d*) As could be expected from the mean flow properties and as has been confirmed by simulations and experiments (Metzler *et al.* 2003), the perturbed flow within the shocked-fluid region, and therefore the interaction between the rippled shock front and the ablation layer, is essentially governed by convection and acoustic wave propagation.

(*e*) The finite extent of the flow is determinant for the evolutions of perturbations of wavelengths comparable to or larger than the distance separating the critical surface from the shock front. In particular, the presence of this bounding shock wave and the resulting confinement of the shocked-fluid region has stimulated laser imprinting models (Ishizaki & Nishihara 1997; Velikovich *et al.* 1998) based on an analogy with the Richtmyer–Meshkov instability (Richtmyer 1960; Meshkov 1969), by contrast to the Rayleigh–Taylor instability analogy commonly invoked for strongly accelerated ablation fronts.

(*f*) The ablation layer is weakly accelerated, or even decelerated (Metzler *et al.* 1999), as compared to the strongly accelerated regime occurring during the shell-acceleration stage. In the presence of a weak destabilizing inertial force field (the layer acceleration), it is expected that the stabilizing and damping mechanisms at work in ablation fronts are noticeably influencing, if not ruling, the layer dynamics. This appears to be effectively the case as laser imprint simulations (Velikovich *et al.* 1998; Goncharov *et al.* 2000; Schmitt *et al.* 2001) exhibit ablation front distortion decaying oscillations for perturbation wavelengths sufficiently small, but much larger than the layer characteristic length. Such a behaviour is recovered by existing modellings (Goncharov *et al.* 2000, 2006), although the best available experimental data (Aglitskiy *et al.* 2002; Metzler *et al.* 2003) do not cover enough oscillations to be conclusive about the actual oscillation frequency and amplitude decay.

Nevertheless other mean flow key features have yet to be adequately addressed by laser imprinting modelling, or even simulations.

Stratification. Since laser asymmetry wavelengths cover the full range spanned by the different flow region characteristic lengths, mean flow stratification and confinement effects must be properly rendered. The currently available laser imprinting model taking into account the flow confinement (Goncharov *et al.* 2000, 2006) is based on a sharp boundary modelling of the ablation layer (Piriz *et al.* 1997) and is consequently improper for describing perturbation evolutions of wavelengths $\lambda_\perp$ larger than the conduction zone size, i.e. $\ell_{con}/\lambda_\perp \lesssim 1$. Other more elaborate ablation front modelling at large Froude numbers (Piriz & Portugues 2003; Sanz, Masse & Clavin 2006), valid in particular for $\ell_{con}/\lambda_\perp < 1$, ignore the bounding shock wave and are therefore of limited usefulness for laser imprinting analysis. As for simulations, accurately rendering stratification imposes drastic constraints on the local computational grid size which are not necessarily met in practice: perturbation wavelengths can be thousands of times larger than the ablation layer characteristic length (see Goncharov *et al.* 2006).

Unsteadiness. The conduction zone and shocked-fluid region thicknesses, as well as the ablation layer characteristic length increase with time (Emery *et al.* 1991; Velikovich *et al.* 1998), and often linearly with time (Goncharov *et al.* 2000, 2006). The fact that in such circumstances, early perturbation growth is found in simulations to be also approximately linear in time (Nishihara *et al.* 1998; Velikovich *et al.* 1998; Metzler *et al.* 1999; Goncharov *et al.* 2000, 2006) casts doubt on results derived from any modelling based on quasi-steady mean flow approximations.

Compressibility. Compressibility may affect ablation front instabilities in several ways (Piriz 2001*b*):

through the stratification of the different flow regions (quantified by the ratio $\gamma\, a\, \ell / c_S^2$ where a denotes an acceleration, ℓ a characteristic length and c_S the isentropic sound velocity);

through the fluid adiabatic exponent γ which enters the fluid acoustic impedance;

through the flow regimes (characterized by local Mach numbers) in the expanding conduction zone and in the ablation layer.

The laser imprinting model of Goncharov *et al.* (Goncharov *et al.* 2000, 2006) which takes into account acoustic wave propagation within the shocked-fluid region, ignores all other compressibility effects since it relies on a sharp boundary ablation front model (Piriz *et al.* 1997) for low-Mach-number flows (Kull & Anisimov 1986). Such a quasi-incompressible flow assumption is not necessarily satisfied throughout the conduction zone in realistic ICF ablative flows (see Piriz 2001*b*). Unfortunately, available investigations of the effects of a compressible conduction zone flow for accelerated (Piriz 2001*b*) or unaccelerated (Piriz & Portugues 2003) ablation fronts are of limited usefulness in laser imprinting configurations since they are restricted to unconfined and steady ablative flows. Laser imprinting numerical simulations which suffer none of the above restrictions, may, however, be questioned with respect to acoustic effect rendering owing to the overly dissipative and dispersive numerical methods commonly used in hydrodynamics codes dedicated to ICF applications.

On the other hand, taking into account the above features which are characteristic of real ICF ablative flows, may be achieved by means of the similarity framework of § 2. For direct laser beam irradiation, the relevance of these similarity solutions to actual ICF pellet ablation flows is bound to the following assumptions.

(i) Electron and ion temperature decoupling within the hot plasma is weak.

(ii) Classical electron heat conduction prevails, i.e. we may take $\mu = 0$, $\nu \simeq 5/2$ in (2.2).

As mentioned by Brun *et al.* (1977), these conditions are best fulfilled during the early irradiation of a material of low atomic number such as the cryogenic deuterium–tritium mixture considered in ICF target designs (Bodner *et al.* 1998). In addition, since the mean flow modelling of § 2 does not include an energy source term as in (2.3), the corresponding solutions omit the subcritical plasma expansion and assume that the (critical) surface of laser energy conversion into heat flux is a material surface – i.e. of zero mass flux. This feature is not met in typical ablative heat waves triggered by laser light irradiation. In that respect, the similarity solutions proposed for a two-temperature fluid model of a plasma (Anisimov 1970; Sanmartín & Barrero 1978*a*) would provide, at the cost of increased complexity, an improvement in the modelling of such flows. A further restriction is imposed by the laser intensity time dependence at the critical surface which must follow (2.7) with the definitions

γ	μ	ν	α
5/3	0	5/2	4/3

TABLE 1. Ablation by direct laser beam illumination. Definitions of the fluid adiabatic exponent γ, heat conduction density and temperature exponents μ and ν, and resulting similarity exponent value α.

(2.12), (2.19). Such a laser intensity temporal law is not representative of current schemes of ICF-pellet early irradiation by laser beams (e.g. see Goncharov *et al.* 2000), although it could be achieved in dedicated experiments. Given these mean flow modelling limitations, the present application of the framework of §§ 2 and 3 to the laser imprinting problem aims at exhibiting qualitative stability behaviours which may be encountered in unsteady compressible ablative flows related to ICF, rather than providing quantitative estimates of perturbation evolutions in actual ICF pellet implosions. Solving with high accuracy the mean flow and perturbation exact equations (2.5), (3.10) – keeping in mind the leading shock-front non-isothermal approximation (§ 2.2) – presents then the advantage of establishing, rather than hypothesizing, which physical features of the flow play determining roles with respect to its stability.

Our laser imprinting analysis of unsteady compressible ablative flows (Abéguilé *et al.* 2006) relies on two self-similar mean flow configurations and their perturbation which we detail in the next two sections (§§ 4.2, 4.3). Temporal response data obtained from integrating (3.10) are then discussed in § 4.4 and are shown to exhibit, provided that the perturbation configuration is properly chosen, the reduction of variables discussed in § 3.2 and established in Appendix A. This result allows us (§ 4.5) to build the reduced response (A 19) for each configuration and to draw firm conclusions. In addition, an illustration (§ 4.6) of possible practical applications is provided by a comparison of ablation front distortion dynamics obtained in different ablative flows. Finally (§ 4.7), we discuss the present findings in connection with available results from simulations and modelling of laser imprinting, as well as from models of ablation fronts at large Froude numbers.

4.2. *Self-similar mean flow configurations*

The approximation of a material critical surface which is peculiar in the ICF context, is consistent with the fluid density being constant along the self-similar flow external boundary $\xi = 0$ ($m = 0$). Instantaneous fluid pressure and heat flux values at the critical surface of a given ablative flow, along with the corresponding local values of the constant R and of the heat conduction coefficient κ_0, are then pertinent for determining the ranges of the similarity solution parameters (2.8). Such values have been extracted – for a monatomic gas and the Spitzer–Härm model of electron heat conduction (see table 1) – from a simulation, with the FCI2 multiple-physics hydrodynamics code (Buresi *et al.* 1986), of a CH planar foil illuminated by a *Laser MégaJoule* laser pulse (Fortin & Canaud 2000). Two particular cases, corresponding to two different times of this CH foil ablation, have thus been selected, yielding the values, via (2.8), of the boundary condition parameters $\mathscr{B}_p$ and $\mathscr{B}_\varphi$ in table 2 (see table 4 for the corresponding dimensional characteristic and reference flow-variable values).

The numerical integration of the associated nonlinear eigenvalue problem (2.14), (2.18), (B 2) results in the solutions shown in figure 2 and characterized by the reduced abscissae ξ_{abl} of the ablation front – as identified to correspond to the minimum of

Configuration	$\mathscr{B}_p$	$\mathscr{B}_\varphi$	ξ_{abl}	ξ_s	L_{tot}	L_{con}	$L_{abl}\,(10^{-3})$	$M_{S\,abl}$	Fr_{abl}	Pe_{abl}
I	0.001	0.026	0.023	0.110	1.23	1.21	0.04	0.075	4.62	3.27
II	0.030	0.257	0.118	0.300	1.08	1.05	1.80	0.159	2.64	3.11

TABLE 2. Examples of self-similar ablative flows relevant to ICF for the parameter set of table 1. Solution boundary condition parameters $\mathscr{B}_p$, $\mathscr{B}_\varphi$, characteristic similarity abscissas ξ_{abl}, ξ_s, flow typical reduced lengths L_{tot}, L_{con}, L_{abl}, and ablation-front characteristic Mach, $M_{S\,abl}$, Froude, Fr_{abl}, and Péclet, Pe_{abl}, numbers.

the density-gradient scale length – and ξ_s of the shock front given in table 2. For each solution, the conduction zone $0 \leqslant \xi < \xi_{abl}$, ablation layer $\xi \simeq \xi_{abl}$, shocked-fluid region $\xi_{abl} < \xi < \xi_s$, and undisturbed fluid region $\xi_s < \xi$, are apparent on the density (figure 2*a*) and temperature (figure 2*c*) reduced function profiles. Strong variations of the reduced fluid particle acceleration $\bar{A}$ (figure 2*e*), of expression

$$\bar{A}(\xi) = (\alpha - 1)\bar{V}(\xi) - \alpha\, \xi\, \mathrm{d}_\xi \bar{V}(\xi),$$

are noticeable across the ablation layers, as well as non-uniformities throughout the conduction zone. In addition, profiles of the isentropic Mach numbers M_S, here defined in terms of the velocity relative to the ablation front $\xi = \xi_{abl}$, or

$$M_S(\xi) = |\bar{V}(\xi) - \bar{V}(\xi_{abl}) - \alpha\, \xi_{abl}/\bar{G}(\xi_{abl})|/\bar{C}_S(\xi), \tag{4.1}$$

with $\bar{C}_S$,the reduced isentropic sound velocity,

$$\bar{C}_S(\xi) = \sqrt{\gamma\, \bar{\Theta}(\xi)}, \tag{4.2}$$

evidence that, for both solutions, the conduction zone expansion is in part supersonic, while a low-Mach-number flow description could be legitimate for a neighbourhood of the ablation layer and for the shocked-fluid region. The existence of a supersonic expansion region is a peculiarity allowed by the assumption of a material critical surface, but is also dependent on the respective values of the solution boundary condition parameters (2.8): subsonic expansions can also be obtained with the present mean flow modelling (cf. Boudesocque-Dubois *et al.* 2008).

This description is completed by the datum of some of the flow typical lengths via their corresponding reduced lengths (table 2), namely the constants:

$$L_{tot} = t^{-\alpha}\, [\bar{x}(m_s, t) - \bar{x}(0, t)]\,, \quad m_s = t^\alpha \xi_s,$$

for the whole disturbed fluid region;

$$L_{con} = t^{-\alpha}\, [\bar{x}(m_{abl}, t) - \bar{x}(0, t)] \equiv t^{-\alpha}\, \ell_{con}(t), \quad m_{abl} = t^\alpha \xi_{abl},$$

for the conduction zone thickness ℓ_{con};

$$L_{abl} = t^{-\alpha}\, \min_x |\mathrm{d}\ln\bar{\rho}/\mathrm{d}x|^{-1} = \min_\xi |\mathrm{d}_\xi \bar{G}|^{-1} \equiv t^{-\alpha}\, \ell_{abl}(t),$$

for the ablation front density-gradient scale length ℓ_{abl};
where the x-coordinate of a point $\xi = m t^{-\alpha}$ is given by

$$\bar{x}(m, t) = t^\alpha \left[\xi/\bar{G}(\xi) + \bar{V}(\xi)/\alpha\right] + \bar{x}(0, 0).$$

In particular, the disparity between the characteristic lengths of the different flow regions is apparent: while the conduction zone (L_{con}) takes over 97 % of the whole

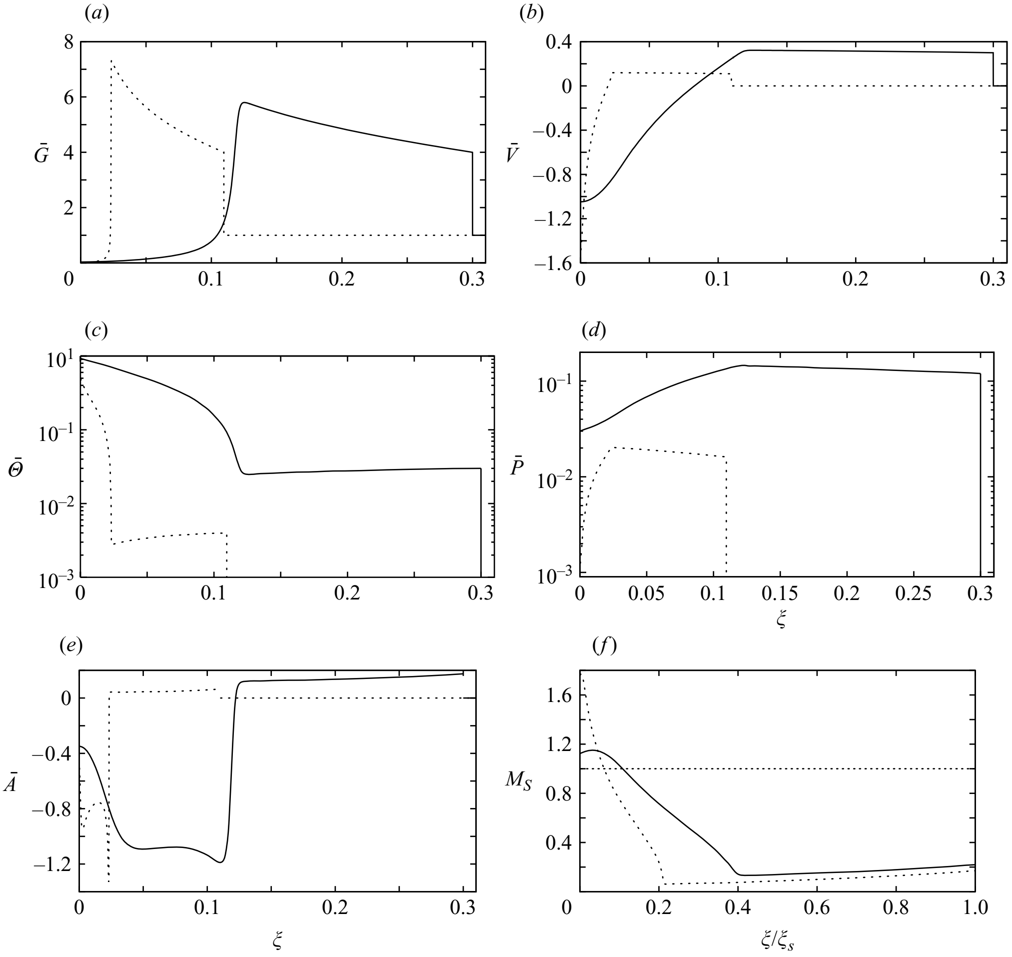

FIGURE 2. Similarity solutions I and II of table 2. Profiles in the self-similar variable ξ of the mean flow reduced (a) density $\bar{G}$, (b) velocity $\bar{V}$, (c) temperature $\bar{\Theta}$, (d) pressure $\bar{P}$, and (e) material acceleration $\bar{A}$. …., I; —, II. The isentropic Mach number, defined by (4.1), which is also represented (f) for both flows as a function of the normalized abscissa ξ/ξ_s, shows that, in each case, a portion of the heat conduction region close to the fluid external boundary $\xi = 0$ is supersonic.

disturbed-fluid region length (L_{tot}), the ablation layer characteristic length (L_{abl}) represents 0.003 % of this length for configuration I *vs.* 0.2 % for configuration II.

These flow ablation layers are further characterized (table 2) by the ablation front isentropic Mach number $M_{S abl} = M_S(\xi_{abl})$, Froude number

$$Fr_{abl} = |\bar{U}_{abl}|/\sqrt{|\bar{A}_{abl}|L_{abl}},$$

and Péclet number

$$Pe_{abl} = \frac{\gamma}{\gamma - 1}\, L_{abl}\, \bar{G}(\xi_{abl})^{1+\mu}\, \bar{\Theta}(\xi_{abl})^{-\nu}\, |\bar{U}_{abl}|,$$

where $\bar{U}_{abl}$ and $\bar{A}_{abl}$ are the reduced ablation velocity and front acceleration, namely

$$\bar{U}_{abl} = -\alpha\xi_{abl}/\bar{G}(\xi_{abl}), \qquad \bar{A}_{abl} = (\alpha - 1)[\bar{V}(\xi_{abl}) - \bar{U}_{abl}]. \tag{4.3}$$

Froude values, for both configurations, are larger than unity, as is usual during the early stage of the shell motion. Péclet values are quite similar in each case and moderate, testifying the comparable importance of energy convection and conduction within the ablation layers.

4.3. *Incident heat flux modulations*

The responses of the self-similar flows of table 2 to incident heat-flux modulations have been investigated by considering, for $t \geqslant t_{ini}$ where t_{ini} is some positive initial time, time-dependent boundary heat-flux perturbations of the form

$$\widehat{\Phi}_{ex}(t) = \Pi(t;\tau)\,\bar{\varphi}_e(t) = \Pi(t;\tau)\,t^{3(\alpha-1)}\,\mathscr{B}_\varphi, \tag{4.4}$$

with

$$\Pi(t;\tau) = 1 - 2/(1+\exp[(t-t_{ini})/\tau]), \quad \tau \geqslant 0, \tag{4.5}$$

in (3.14). As $(t - t_{ini})/\tau$ becomes larger, $\widehat{\Phi}_{ex}(t)/\bar{\varphi}_e(t) \to 1^-$, so that the perturbed configuration becomes that of a unit relative laser-intensity asymmetry. Note that this limiting perturbation configuration is consistent with irradition asymmetries such as laser beam non-uniformities, mispointing or imbalance which are proportional to the instantaneous laser intensity.

In accordance with the identification of the fluid external boundary with the critical surface, the boundary density perturbation is taken to be identically zero in (3.13). Consequently, linear perturbation evolutions are obtained by numerical integration of system (3.10), starting from zero initial perturbations at $t = t_{ini}$, with boundary conditions (3.13) where $\widehat{G}_e = 0$, (3.14) with (4.4) and (3.15), and (B 5) with $\widehat{\boldsymbol{Z}}_U = \boldsymbol{0}$. Depending on the type of computations being performed, the bounds of the integration-time range $[t_{ini}, t_{end}]$ are either independent of the perturbation wavenumber $k_\perp$ being treated, or different for each wavenumber value. Typical computations involve about 10 spectral domains of 50 collocation points each, and may represent several millions of integration time-steps.

4.4. *Fourier mode temporal responses*

Linear perturbation responses are primarily analysed in terms of the absolute density perturbation Fourier mode $\widehat{G}$, since this quantity determines the areal mass perturbations measured in experiments (e.g. see Aglitskiy *et al.* 2002). As an indicator of the global flow response we have retained the density perturbation overall flow extremum

$$|\widehat{G}|_{max}(k_\perp, t) = \max_{\xi} |\widehat{G}(\xi, k_\perp, t)|, \tag{4.6}$$

whereas the density perturbation ablation front value

$$\widehat{G}_{abl}(k_\perp, t) = \widehat{G}(\xi_{abl}, k_\perp, t), \tag{4.7}$$

is used to characterize the ablation layer dynamics. This latter quantity determines the ablation front distortion amplitude as given by the linear deformation of the iso-density surface of equation $\rho(x, y, z, t; \varepsilon) = \bar{G}(\xi_{abl})$, namely

$$\widehat{X}_{abl}(k_\perp, t) = -L_{abl}\,\frac{t^\alpha}{\bar{G}(\xi_{abl})}\,\widehat{G}_{abl}(k_\perp, t). \tag{4.8}$$

From this expression, the ablation front distortion is seen to be proportional to the ablation layer density-gradient length L_{abl}, and to the local mean-flow strain as measured by the partial derivative $\partial\bar{x}/\partial\xi \equiv t^\alpha/\bar{G}$.

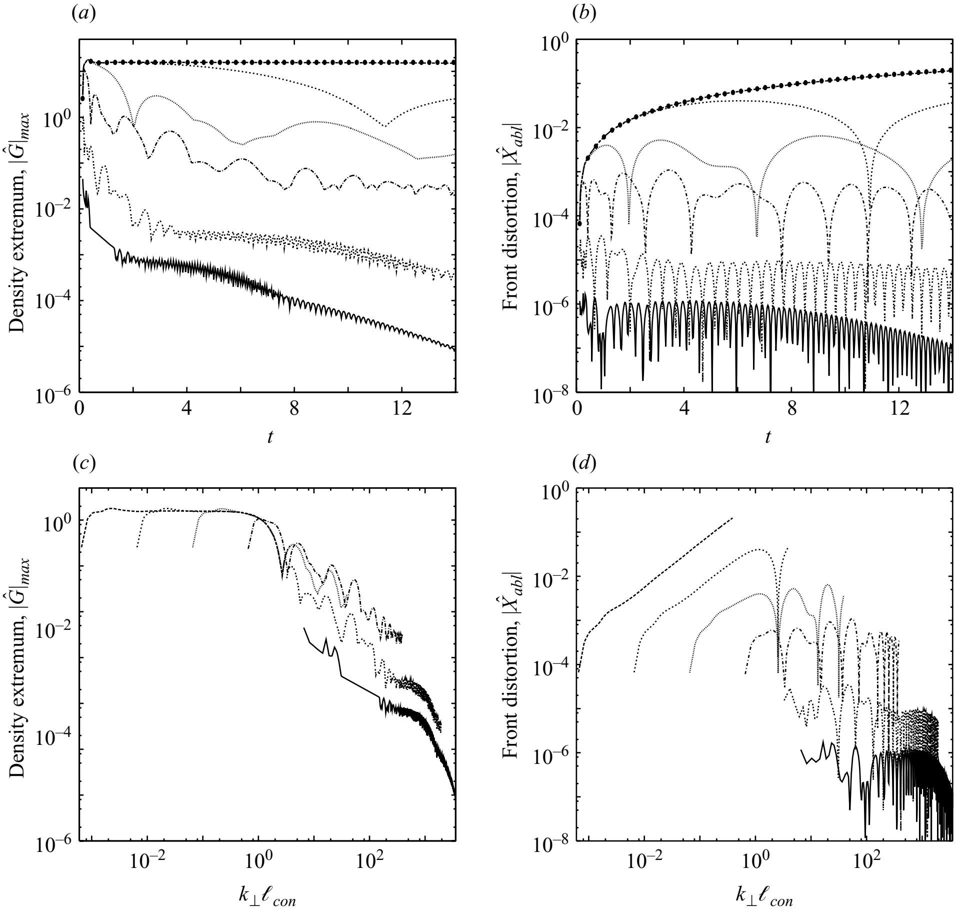

FIGURE 3. Temporal responses of configuration II of table 2 for incident heat-flux perturbation rise-time $\tau = 0.01$ in (4.5), and time $0.1 \leqslant t \leqslant 14$. Evolution of the density perturbation overall flow extrema $|\widehat{G}|_{max}$ as a function of (*a*) time and (*c*) conduction zone relative thickness $k_\perp \ell_{con}$. Evolution of the ablation front distortions $\widehat{X}_{abl}$, given by (4.8), as a function of (*b*) time and (*d*) conduction zone relative thickness $k_\perp \ell_{con}$. Results obtained for (*a*, *b*, from top to bottom; *c*, *d*, from left to right) wavenumbers $k_\perp = 0$ (• of *a*, *b* only), 0.01, 0.1, 1, 10, 50 and 100. The $k_\perp = 100$ data correspond, for the largest values of $k_\perp \ell_{con}$, to wavelengths approaching the ablation layer characteristic length ℓ_{abl} (cf. table 2). Notice the disparity – up to seven decades in perturbation amplitude for wavenumbers spanning four decades – in flow responses that may be captured by the present high-accuracy numerical approach.

4.4.1. *Spectral and temporal variable representation*

Computations of the flow temporal responses in both configuration I and II, over a given time range ($0.1 \leqslant t \leqslant 14$), for several values of the heat-flux perturbation rise-time ($\tau = 1/6$, 0.01, 0), and for wavenumbers $k_\perp$ ranging from 0 to 100, lead to the following findings. After an early time transient, inherent to the progressive perturbation of the whole flow and to the heat-flux perturbation rise-time, density non-uniformities, as illustrated by the evolutions (figure 3*a*) of the overall flow density extrema $|\widehat{G}|_{max}(k_\perp, t)$, are first seen to stagnate for sufficiently short times and small wavenumbers (figure 3*a*, curves $k_\perp \leqslant 0.1$), and, as time increases, to oscillate (figure 3*a*, curves $k_\perp \geqslant 1$) with decaying amplitudes for large enough $k_\perp$. As $k_\perp$ increases, the stagnation phase duration, oscillation periods and flow response magnitude decrease. The corresponding ablation front distortion evolutions (figure 3*b*) exhibit three distinct regimes as determined by the behaviours of $\widehat{G}_{abl}(k_\perp, t)$ through formula (4.8). Hence the density perturbation stagnation phase induces a regime of front distortion algebraic growth (figure 3*b*, curves $k_\perp \leqslant 0.1$), more precisely in $t^{4/3}$ since $\alpha = 4/3$ (cf. table 1), whereas an oscillatory regime of amplitude modulation is discernable for intermediate wavenumbers (figure 3*b*, curves $k_\perp = 1$, 10, 50), leaving place at smaller wavelengths to a damped oscillatory regime (figure 3*b*, curves $k_\perp = 50$ and 100).

4.4.2. *Reduced variable representation*

Analysing such results in terms of the relative size of the conduction zone, $k_\perp \ell_{con} \equiv k_\perp\, L_{con}\, t^{4/3}$, rather than the time t (figures 3*c, d*), highlights the physical importance of this mean flow parameter for laser imprinting. The different regimes of the flow and ablation front responses appear to correspond, for any wavelength, to given ranges of this conduction zone relative thickness. In particular, we recover the known rough features of laser imprinting as identified by previous simulations and modellings – namely, the existence of a front distortion growth regime for $k_\perp \ell_{con} < 1$, and of an oscillatory damped regime for $k_\perp \ell_{con} > 1$ (see figure 3*d*). Similarly, the significant reduction in flow non-uniformity as the conduction zone relative thickness, $k_\perp l_{con}$, at which the laser intensity modulation starts to be applied is increased (figures 3*c, d*), points out the effectiveness of thermal smoothing (Emery *et al.* 1991) in laser imprinting. However the present results have no precedent in terms of details and accuracy, notably in the range of relative wavelengths that is covered. In particular, an example is given of ablation flow responses for wavelengths approaching the ablation layer density-gradient scale length: cf. the curves $k_\perp = 100$ of figures 3(*c, d*).

4.4.3. *From Fourier mode temporal responses to reduced Fourier mode responses*

A more complete description of the flow responses is achieved upon considering computations over fixed ranges of the conduction zone relative thickness $k_\perp \ell_{con}$. Moreover, by choosing the heat-flux perturbation rise-time τ in (4.4) to be zero, the definition of $\widehat{\Phi}_{ex}(t)$ becomes compatible with the perturbation variable reduction relations (3.17), provided that the equation

$$(\delta + 2)(\alpha - 1) + 2\alpha = 3(\alpha - 1),$$

obtained after (3.17), (3.19) and (4.4), is satisfied, or, equivalently, that the free parameter δ of (3.17), (3.18) is given by

$$\delta = -\frac{\alpha + 1}{\alpha - 1}. \tag{4.9}$$

Would the perturbation variable reduction (3.17) be achieved by the numerical solution of the IBVP (3.10)–(3.15), (B 5), the following relations should hold:

$$\widehat{G}(\xi, k_\perp, t) = \widehat{\mathscr{G}}(\xi, k_\perp t^\alpha), \tag{4.10a}$$

$$t^{1-\alpha}\, \widehat{V}_x(\xi, k_\perp, t) = \widehat{\mathscr{V}}_x(\xi, k_\perp t^\alpha), \tag{4.10b}$$

$$t\, \widehat{D}_\perp(\xi, k_\perp, t) = \widehat{\mathscr{D}}_\perp(\xi, k_\perp t^\alpha), \tag{4.10c}$$

$$t^{2(1-\alpha)}\, \widehat{\Theta}(\xi, k_\perp, t) = \widehat{\mathscr{T}}(\xi, k_\perp t^\alpha), \tag{4.10d}$$

$$t^{2(1-\alpha)}\, \widehat{P}(\xi, k_\perp, t) = \widehat{\mathscr{P}}(\xi, k_\perp t^\alpha), \tag{4.10e}$$

with $\alpha = 4/3$.

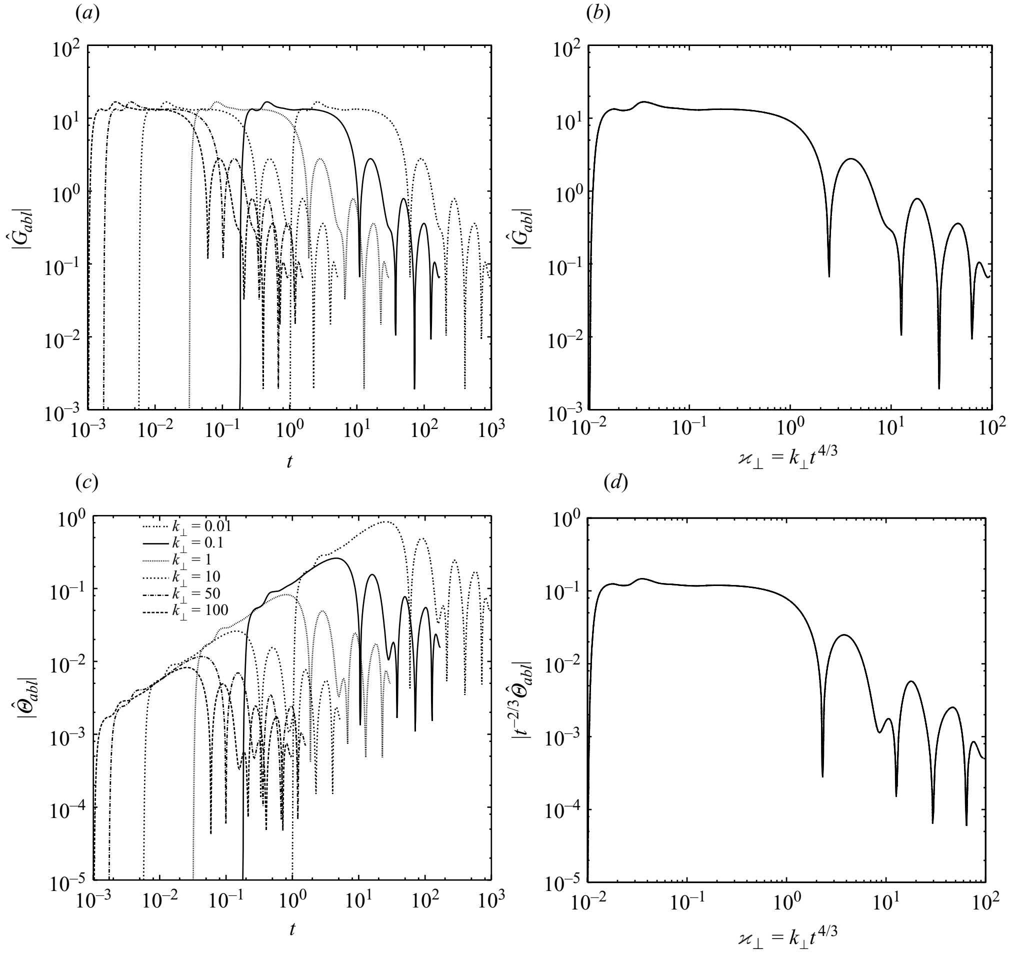

FIGURE 4. Temporal responses of configuration II of table 2 for incident heat-flux perturbation rise-time $\tau = 0$, and time t such that $10^{-2} \leqslant L_{con} k_\perp t^{4/3} \leqslant 10^2$. Ablation front density perturbations $\widehat{G}_{abl}$ as a function of (a) time and (b) reduced wavenumber $\varkappa_\perp = k_\perp t^{4/3}$. Ablation front ($c$) temperature perturbations $\widehat{\Theta}_{abl}$ as a function of time, and (d) reduced temperature perturbation temporal equivalent, $t^{-2/3}\,\widehat{\Theta}_{abl}$, as a function of the reduced wavenumber $\varkappa_\perp = k_\perp t^{4/3}$. Results obtained for $k_\perp = 0.01$, 0.1, 1, 10, 50 and 100. The superposition of the results when plotted *vs.* $\varkappa_\perp$ (b, d) shows the variable reduction defined by (4.10).

For non-zero wavenumbers, time-integration results computed over the same range of the parameter $\varkappa_\perp = k_\perp t^{4/3}$ but for different values of $k_\perp$, present the characteristics of the variable reduction as stipulated by the above relations. Indeed, past an initial transient set-up of perturbations throughout the flow, computed values of the left-hand sides of (4.10) recorded, for different non-zero $k_\perp$, as functions of $k_\perp t^{4/3}$, are found to agree within the accuracy limits allowed by discrepancies in the $k_\perp t^{4/3}$ variable sampling; see figure 4 for an illustration in the configuration II case.

For zero wavenumber ($k_\perp = 0$), computed temporal responses (not shown) turn out, for sufficiently long integration times, to possess the similarity defined by (4.10a, b, d, e) which is merely that of the mean flow (2.13). Given that the boundary heat-flux perturbation (4.4), (4.5) for $\tau = 0$ comes down to a shift of the parameter $\mathscr{B}_\varphi$ of (2.8),

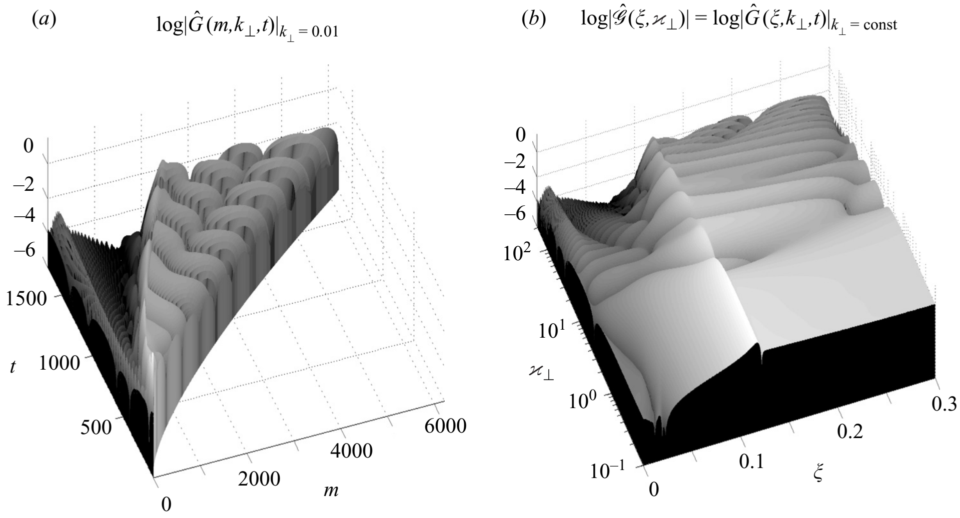

FIGURE 5. Temporal and reduced responses of configuration II of table 2. Amplitude plot (*a*) in the (m, t) variables of the temporal density perturbation response $\widehat{G}(\xi, k_\perp, t)$ obtained at a wavenumber value of $k_\perp = 0.01$, with an incident heat-flux perturbation rise-time $\tau = 0$, and for times t such that $0.01 \leqslant \varkappa_\perp \leqslant 210$. Corresponding representation (*b*) in the $(\xi, \varkappa_\perp)$ variables of the associated reduced response $\widehat{\mathscr{G}}(\xi, \varkappa_\perp)$ as obtained over the partial range $0.1 \leqslant \varkappa_\perp \leqslant 210$ by means of (4.10*a*) taken for a given value of $k_\perp$. The fluid external surface and shock-wave front located, respectively, at $\xi = 0$ and $\xi = \xi_s = 0.3$ in (*b*), correspond, respectively, to the lower and upper m-coordinate boundaries in (*a*). In both plots, the ablation layer appears as the ridge of maximum perturbation amplitude.

and that the zero boundary density perturbation in (3.13) is compatible with the laws (2.13), the resulting (nonlinearly) perturbed flow may be expected to obey the same similarity. The above linear perturbation temporal response results confirm this, at leading order in the perturbation amplitude, thus suggesting that both configurations I and II are linearly stable with respect to one-dimensional perturbations. The long-time constant behaviour of the density perturbation and $t^{4/3}$ growth of the ablation front deformation at zero wavenumber, shown in figure 3(*a, b*) and discussed in the preceding sections, are a mere transcription of this fact.

Such results show that, for the present mean flow configurations, the perturbation temporal responses (3.9) converge, via the relations (4.10), towards the reduced responses (A 19), so that the latter may be held as attractors for the solutions of the temporal PDE system (3.10). Consequently, we are able to determine the perturbation reduced responses (A 19), over a given range $[\varkappa_{\perp min}, \varkappa_{\perp max}]$, $\varkappa_{\perp min} > 0$, of the reduced wavenumber $\varkappa_\perp \equiv k_\perp t^{4/3}$, by means of a single, properly tailored, temporal response computation at a particular non-zero wavenumber $k_\perp$, and for $\varkappa_\perp = 0$ by a sufficiently long-time computation at $k_\perp = 0$.

4.5. *Reduced Fourier mode responses*

4.5.1. *Overall flow responses*

An example of reduced responses in the configuration II case is given in figures 5(*b*) and 6 under the form of plots – over the full extent of the flow, $0 \leqslant \xi \leqslant \xi_s = 0.3$, in the reduced space variable ξ and over the reduced wavenumber range $0.1 \leqslant \varkappa_\perp \leqslant 210$ – of the five perturbation reduced Fourier modes of (4.10). Care was taken in choosing, for

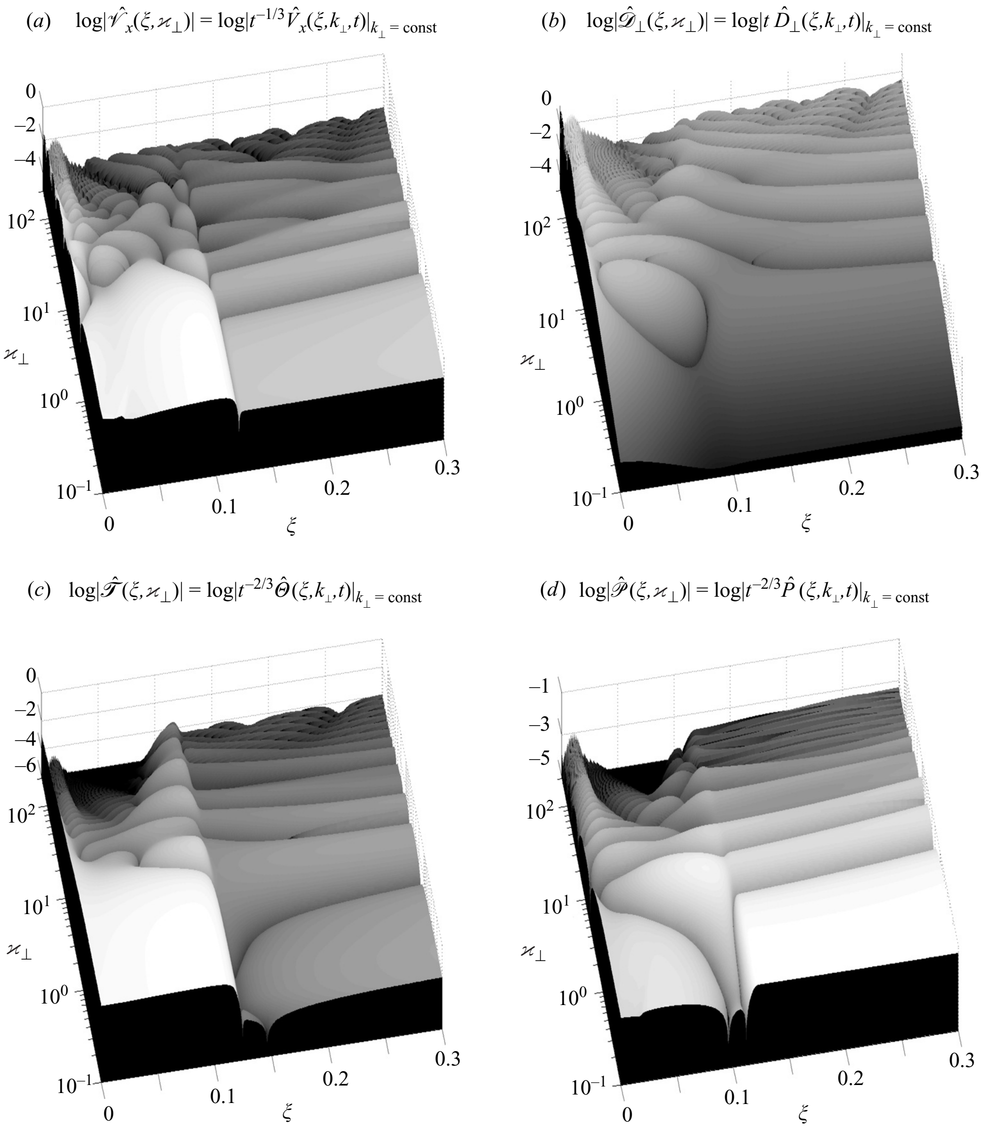

FIGURE 6. Reduced responses of configuration II of table 2. Amplitude plots in the $(\xi, \varkappa_\perp)$ variables of the reduced perturbation responses for (*a*) the x velocity $\widehat{\mathscr{V}}_x$, (*b*) the transverse expansion $\widehat{\mathscr{D}}_\perp$, (*c*) the temperature $\widehat{\mathscr{T}}$, and (*d*) the pressure $\widehat{\mathscr{P}}$ over the whole flow reduced extent $0 \leqslant \xi < 0.3$ and the reduced wavenumber range $0.1 \leqslant \varkappa_\perp \leqslant 210$. The ablation layer located about $\xi \simeq 0.12$ is noticeable in the x-velocity (*a*), temperature (*c*) and pressure (*d*) responses by more or less pronounced sharp amplitude variations. The conduction zone $(0 \leqslant \xi \lesssim 0.12)$ is characterized by an important damping of temperature perturbations as $\varkappa_\perp$ increases (*c*), with the noticeable exceptions of the supersonic expansion region $(\xi \lesssim 0.03)$ and of the vicinity of the ablation layer. Pressure perturbations (*d*) are seen to build up within this supersonic region for increasing $\varkappa_\perp$, while their arrangement, for large enough $\varkappa_\perp$, along lines $(\xi \nearrow, t \nearrow)$ and $(\xi \searrow, t \nearrow)$ within the shocked-fluid region $(0.12 \lesssim \xi < 0.3)$ is indicative of acoustic waves propagating back and forth between the conduction zone and the shock front.

the corresponding temporal response computation, a sufficiently small initial time t_{ini} so that, by the time t at which $\varkappa_\perp = k_\perp t^{4/3} = 0.1$, the influence of the perturbation initial transient set-up could be held as negligible. Single-mode temporal or instantaneous spectral response data are thus available throughout the whole flow by considering either $k_\perp$, or t, to have a fixed non-zero value.

Hence for some particular non-zero wavenumber, the reduced response representations in figures 5(*b*) and 6 determine, via (4.10), the time evolution, in the mean-flow reduced space, of perturbations between the fluid external surface, $\xi = 0$, at which the laser intensity modulation is applied, and the fore-running shock front at $\xi = \xi_s$. The correspondence between such a representation and that obtained in the more physically representative variables m and t is illustrated in the case of the density perturbation $\widehat{G}$ by figure 5(*a*, *b*). In figure 5(*a*), the trajectories $m = 0$ of the fluid external surface and $m = \xi_s \, t^{4/3}$ of the shock front – visible as the upper-m edge of the plotted surface – are mapped, respectively, into the boundaries $\xi = 0$ and $\xi = \xi_s = 0.3$ of the $(\xi, \varkappa_\perp)$ domain in figure 5(*b*). The ablation layer identified in figure 5(*a*) by the ridge of density perturbation amplitude, is found in figure 5(*b*) about the straigth line $\xi \simeq 0.12$. Owing to the mean flow dilatation, the perturbation amplitude fluctuation spatial frequency, whether in the m or ξ variable, increases with time, and more markedly in the conduction zone than in the shocked-fluid region, in accordance with the flow region respective dilatations in the x-coordinate system given by the associated reduced lengths (see table 2). For the particular case $k_\perp = 0$, the reduced response data are simply given by the long-time values of the reduced perturbation temporal equivalents found on the left-hand sides of (4.10*a*, *b*, *d*, *e*).

At any given non-zero time, the same reduced responses obtained for $\varkappa_{\perp min} \leqslant \varkappa_\perp \leqslant \varkappa_{\perp max}$ yield, through a mere rescaling of the spectral and response variables, the perturbation spectra over the wavenumber range $\varkappa_{\perp min} t^{-\alpha} \leqslant k_\perp \leqslant \varkappa_{\perp max} t^{-\alpha}$, with a wavenumber resolution given by the time-integration data recording rate. As in the temporal response case, the desired spectral data points at $k_\perp = 0$ are provided by the corresponding temporal response long-time computation.

We leave for future work a detailed analysis of perturbation fluctuation patterns such as those displayed in figures 5 and 6. Nevertheless, several features of these patterns are worth mentioning. Temperature perturbations (figure 6*c*) throughout the conduction zone ($0 \leqslant \xi < 0.12$), but away from the supersonic expansion region ($0 \leqslant \xi \lesssim 0.03$) and the ablation layer ($\xi \simeq 0.12$), are noticeably damped for large $\varkappa_\perp$ as could be expected from the thermal smoothing taking place in this region. The supersonic expansion region, noticeable in each of the five flow variable perturbation responses $\widehat{\mathscr{G}}$, $\widehat{\mathscr{V}}_x$, $\widehat{\mathscr{D}}_\perp$, $\widehat{\mathscr{T}}$, $\widehat{\mathscr{P}}$ (figures 5*b*, 6), is particularly apparent in terms of pressure perturbations (figure 6*d*), suggesting a trapping of acoustic waves of sufficiently short wavelengths within this portion of the flow. Within the shocked-fluid region ($0.12 \lesssim \xi < 0.3$), acoustic waves, as witnessed by pressure perturbation fluctuations (figure 6*d*), propagate back and forth between the shock-wave front and the conduction zone, including the ablation layer, the dynamics of these regions possibly interfering with each other. This acoustic reverberation maintains itself for larger values of $\varkappa_\perp$ than the interaction between the critical surface and the ablation layer does, as could be expected from the smaller size of the shocked-fluid region ($L_{tot} - L_{con} \simeq 0.03$) as compared to the conduction zone extent ($L_{con} = 1.05$), and from the large level of heat diffusion within the conduction zone.

4.5.2. *Ablation front responses*

Taking full advantage of the temporal response variable reduction (4.10), reduced responses for both configurations I and II have been determined for extended ranges of the reduced wavenumber $\varkappa_\perp$ (see table 3). In the configuration II case, the reasonably small value of the ratio $L_{abl}/L_{tot} \simeq 2 \times 10^{-3}$ (cf. table 2) has permitted the computation

	$\varkappa_{\perp min}$	$\varkappa_{\perp max}$
I	0.01	210
II	0.01	3 491

TABLE 3. Reduced wavenumber ranges for the reduced responses of configurations I and II of table 2.

of perturbations up to times where the ablation front characteristic length exceeds the perturbation wavelength: the chosen value of $\varkappa_{\perp max}^{\mathrm{II}}$ in table 3 is such that $\ell_{abl}(t_{end})/\lambda_\perp > 1$. In the configuration I case, an equivalent computation would be far too demanding in terms of spatial resolution and number of integration time steps owing to the much smaller ratio $(L_{abl}/L_{tot})^{\mathrm{I}} \simeq 3 \times 10^{-5}$ (cf. table 2), whence the moderate value of $\varkappa_{\perp max}^{\mathrm{I}}$ retained in table 3.

The corresponding results are analysed in terms of the reduced density perturbation overall flow extremum and ablation front values, i.e.

$$|\widehat{\mathscr{G}}|_{max}(\varkappa_\perp) = \max_{\xi} |\widehat{\mathscr{G}}(\xi, \varkappa_\perp)|, \quad \widehat{\mathscr{G}}_{abl}(\varkappa_\perp) = \widehat{\mathscr{G}}(\xi_{abl}, \varkappa_\perp), \tag{4.11}$$

as functions of $k_\perp \ell_{con} \equiv \varkappa_\perp L_{con}$. These responses (figure 7) show that, for the present flows:

(i) Both $|\widehat{\mathscr{G}}|_{max}(\varkappa_\perp)$ and $|\widehat{\mathscr{G}}_{abl}(\varkappa_\perp)|$ are almost constant for $k_\perp \ell_{con} \lesssim 0.1$, and bounded from above by their respective values at $\varkappa_\perp = 0$ (see figure 7 *a,b*). In particular, we have

$$|\widehat{\mathscr{G}}_{abl}(\varkappa_\perp)| \simeq \mathrm{const} \leqslant |\widehat{\mathscr{G}}_{abl}(0)|. \tag{4.12}$$

The same feature is verified at different flow locations, as well as for the other fluid quantity reduced perturbations $\widehat{\mathscr{V}}_x$ and $\widehat{\mathscr{T}}$, thus indicating that the mean flow self-similar character dominates the perturbation evolution, not only for purely longitudinal perturbations, i.e. at $k_\perp = 0$ (see § 4.4.3), but also for sufficiently small perturbation reduced wavenumbers. The corresponding three-dimensional perturbed flow may then be pictured roughly as consisting of one-dimensional flows proceeding independently along each line of constant (y, z) according to the particular self-similar solution defined by the perturbed boundary conditions at the point $(m = 0, y, z)$. Such a quasi-one-dimensional motion description is qualitatively reasonable as long as: (*a*) a significant amount of the ablative flow driving source – in effect the external boundary heat flux – perturbation is transmitted to the entire flow, and (*b*) the perturbation transverse flow has not yet reached significant levels. Early investigations of laser illumination non-uniformities (e.g. see Brueckner & Jorna 1974) predicted that boundary heat-flux perturbation transmission at the ablation layer should roughly cease to be effective for wavelengths approaching the conduction zone size, i.e. for $k_\perp \ell_{con} \simeq 2\pi$. The present results are consistent with such a prediction: the data in figure 3 indicate that ablation front perturbations may be decreased by one (two) order(s) of magnitude upon applying the same heat flux perturbation for $k_\perp \ell_{con} \gtrsim 5$ (respectively, $k_\perp \ell_{con} \gtrsim 10$) – cf. the curves for $k_\perp = 50$ (respectively, $k_\perp = 100$) – rather than for $k_\perp \ell_{con} < 1$ (curves for $k_\perp = 10$). Perturbation coupling between the ablation front and the flow external boundary is thus marginal for $k_\perp \ell_{con} \gtrsim 5$, and negligible for $k_\perp \ell_{con} \gtrsim 10$. However ablation-front perturbations are seen to depart

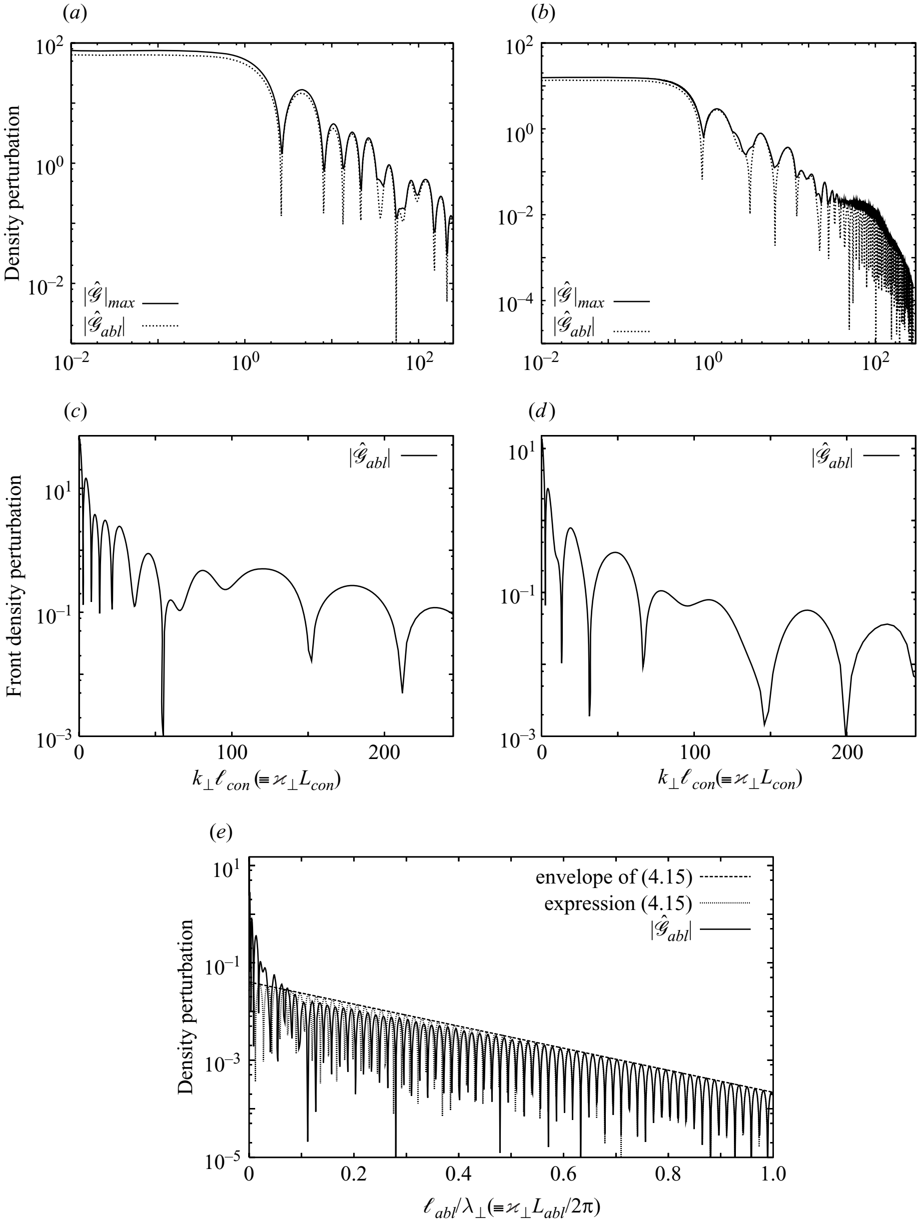

FIGURE 7. Reduced responses of configurations I and II of table 2 over the reduced wavenumber ranges of table 3. Overall flow extrema $|\widehat{G}|_{max}$ (a, b only) and ablation front values $\widehat{\mathscr{G}}_{abl}$ of the density perturbation reduced responses *vs.* the relative conduction zone size, $k_\perp \ell_{con}$, for configurations (a, c) I and (b, d) II, and (e) proof, in the configuration II case, of the damped oscillatory behaviour (4.15) of $\widehat{\mathscr{G}}_{abl}$ in the limit $\ell_{abl}/\lambda_\perp \to 1^-$. In ($e$) the comparison is based on a determination of the constants in (4.15) by a least-squares fit of the data $\widehat{\mathscr{G}}_{abl}(\varkappa_\perp)$ over the range $0.7 \leqslant \varkappa_\perp L_{abl}/2\pi \leqslant 1$. The corresponding computations involve, respectively, over 11×10^6 and over 8×10^6 time integrations of system (3.10) for configuration I and II.

significantly from the self-similar behaviour $\widehat{\mathscr{G}}_{abl}(\varkappa_\perp) = \text{const}$, for values of $k_\perp \ell_{con}$ as low as 0.5 (figure 7a, b), i.e. for $\lambda_\perp < 0.1\,\ell_{con}$, although heat-flux perturbation transmission throughout the conduction zone is still effective at this stage (see the reduced temperature perturbation response in figure 6*c*). Such a departure for the reduced temperature and pressure perturbations (figure 6*c*, *d*) are first observed in the vicinity of the ablation layer: noticeable variations with respect to $\varkappa_\perp$ appear, for $\varkappa_\perp \lesssim 1$, in the region $0.1 < \xi < 0.15$. Quite differently, the perturbation transverse flow (figure 6*b*) builds up mainly in the conduction zone region close to the external surface as well as, to a weaker extent, downstream of the shock front. Hence, the perturbed flow departure from its quasi-one-dimensional self-similar motion originates from three distinct regions: the flow external surface; the ablation layer; and the leading shock front. This description is not qualitatively different from those given by previous studies of realistic ICF laser-imprint configurations (cf. § 4.1).

A noteworthy consequence of the mean flow self-similarity dominance on the perturbation evolution at long wavelengths, is that perturbations evolve over a characteristic time, say $\mathrm{t}_\perp$, comparable to the mean flow evolution time t, namely,

$$\mathrm{t}_\perp \simeq \mathrm{t} = 3\,t/4. \tag{4.13}$$

This shows the critical influence of the mean flow unsteadiness at this stage. The flow compressibility also comes out to be determinant in that the ablation front characteristic time $\mathrm{t}_{\perp abl}$ remains smaller than the acoustic transit time $\lambda_\perp / c_{S\,abl}$; we have, for $k_\perp\, \ell_{con} = \varkappa_\perp\, L_{con} < 1$,

$$\frac{\mathrm{t}_{\perp abl}}{\lambda_\perp / c_{S\,abl}} \simeq \frac{\mathrm{t}}{\lambda_\perp / c_{S\,abl}} = \frac{3}{8\pi}\, \bar{C}_S(\xi_{abl})\, \varkappa_\perp < 1, \tag{4.14}$$

where $\bar{C}_S(\xi_{abl})$ is given by (4.2).

(ii) For $k_\perp \ell_{con} > 1$, $|\widehat{\mathscr{G}}|_{max}(\varkappa_\perp)$ and $\widehat{\mathscr{G}}_{abl}(\varkappa_\perp)$ undergo damped oscillations as $\varkappa_\perp$ increases (figure 7*a*, *b*). In effect, two subregions of the $\varkappa_\perp$ spectrum may be identified.

(*a*) For moderate values of $\varkappa_\perp$ (cf. figure 7*c*, *d*, for $1 < \varkappa_\perp L_{con}$), $\widehat{\mathscr{G}}_{abl}$ displays oscillatory behaviours which do not reduce to damped monochromatic sinusoidal oscillations. At this stage, the shock front and ablation layer are no more than a wavelength apart and therefore strongly interfere with each other (see figures 5*b* and 6*d*). Comparatively, the coupling between the external boundary and the ablation layer is much weaker and presents a faster decrease with $\varkappa_\perp$, as shown by the respective levels of reduced temperature and pressure perturbations within the conduction zone and the shocked-fluid region (see figure 6*c*, *d*). In that respect, the presence of supersonic expansion regions close to the flow external boundaries $m = 0$ contributes to this increased decoupling: perturbations introduced at $m = 0$ may reach the ablation layer only by means of thermal diffusion since the upstream propagation of acoustic-type fluctuations is inhibited in these regions.

Comparison of $\mathrm{t}_{\perp abl}$, as estimated from periods between consecutive phase reversals of $\widehat{\mathscr{G}}_{abl}$, with the mean-flow characteristic time t reveals that the mean-flow unsteadiness influence gradually decreases, the threshold value $\mathrm{t}_{\perp abl}/\mathrm{t} = 0.1$ below which a mean-flow quasi-steady assumption may be locally justified, being reached for $\varkappa_\perp L_{con} \simeq 211$ ($\varkappa_\perp L_{con} \simeq 200$, equivalently $\ell_{abl}/\lambda_\perp \simeq 0.06$) in configuration I (respectively, configuration II) case. Oscillation pseudo-frequencies associated to $\mathrm{t}_{\perp abl}$, evolve then, for configuration I (configuration II), from values significantly larger than (respectively, slightly larger than), to values slightly larger (respectively, smaller, but not much smaller) than the acoustic frequency $c_{S\,abl}\, k_\perp$. Hence, if the perturbation flow compressibility decreases in both cases, it stays high in the configuration I case, and remains significant for configuration II. This feature is to be related with the proximity of the shock-wave front at this point of the flow evolutions.

(*b*) For larger values of $\varkappa_\perp$ (configuration II, see figure 7*e* for $\ell_{abl}/\lambda_\perp \gtrsim 0.1$) ablation-front density oscillations become the damped sinusoidal type. This regime corresponds to distances between the shock front and the ablation layer increasing from 1 to 17 perturbation wavelengths. The interaction between the dynamics of these two fronts, under the form of acoustic wave reverberation and downstream convection of vorticity and entropy perturbations initiated at the shock front, is thus weakening. Reduced density perturbation $\widehat{\mathscr{G}}_{abl}$ evidences then, as the ablation layer characteristic length ℓ_{abl} becomes comparable to the perturbation wavelength $\lambda_\perp$, i.e. in the limit $\ell_{abl}/\lambda_\perp \to 1^-$, an exponentially damped oscillatory behaviour of the form (see figure 7*e*)

$$\widehat{\mathscr{G}}_{abl}(\varkappa_\perp) \sim \operatorname{Re}\{a_0 \exp[(-\sigma + \mathrm{i}\omega)\varkappa_\perp]\}, \tag{4.15}$$

where a_0 is a complex constant, and σ, ω two real positive constants.

Throughout this regime, oscillation frequencies remain sufficiently high with respect to the acoustic frequencies (in a ratio of about 1/3) so that the perturbation flow compressibility, under the form of acoustic effects, cannot be neglected.

Damped oscillations of ablation fronts are predicted by the low-Mach-number sharp boundary modelling of laser imprinting (Goncharov *et al.* 2000, 2006). However, the applicability of such a modelling to the present flow configurations is restricted by at least two of its underlying assumptions. One is the low-Mach-number ablative flow approximation which is improper for describing the outermost portions of the heat conduction zone expansions, and therefore imposes a lower bound on the perturbation wavenumber spectrum that may be considered. The other is the steady mean-flow approximation which, as found above, is here only justified for wavelengths much smaller than the conduction zone size. Another limitation is the neglect of the ablation and shock-front accelerations, whereas the self-similar flows of table 2 involve accelerating ablation layers and shock fronts. Estimates obtained in this context should thus be taken with some caution. In (Goncharov *et al.* 2006, equation 49), ablation front perturbation oscillations are described as originating from three different types of sources, each being associated to a typical frequency.

(i) *Acoustic waves emitted by the rippled shock front*, with induced frequencies corresponding roughly to the local acoustic frequency, here $c_{S_{abl}}\, k_\perp = \bar{C}_S(\xi_{abl})\, k_\perp\, t^{1/3}$.

(ii) *Vorticity and entropy perturbations left out by the rippled shock front*, of associated frequencies given, in the present cases, by the formula

$$\frac{4}{3}\,\frac{\sqrt{1 - M_{S_D}^2}}{M_{S_D}}\,\frac{\bar{G}_{abl}}{\bar{G}_D}\,\bar{U}_{abl}\, k_\perp\, t^{1/3}, \tag{4.16}$$

where $\bar{U}_{abl}$ is the reduced ablation velocity (4.3), $\bar{G}_D$ the reduced density value downstream of the shock front, and M_{S_D} the relative flow Mach number at this very location.

(iii) *Ablation front stabilization due to the so-called 'rocket effect', or dynamic overpressure mechanism* (Sanz 1996; Piriz *et al.* 1997), with corresponding frequencies at present estimated by the expression

$$\bar{U}_{abl}\,(L_0\, k_\perp\, t^{4/3})^{-1/2\nu} k_\perp\, t^{1/3}, \tag{4.17}$$

where $L_0 = \nu^\nu(\nu + 1)^{-(\nu+1)}\, L_{abl}$ and $\nu = 5/2$.

These formulae should, in principle, be applied within the reduced wavenumber range $2\pi/L_{con} \ll \varkappa_\perp \ll 2\pi/L_0$ (sharp boundary model restriction) provided that $\mathrm{t}_{\perp abl}/\mathrm{t} \ll 1$ (stationary mean flow approximation). Under these restrictions, oscillation pseudo-frequencies in the configuration II case are found to be, consistently, at most 30 % below the vorticity/entropy frequency (4.16), while being, as $\varkappa_\perp$ become larger, increasingly higher (from 1.3 times to 2 times) than the rocket-effect frequency estimate (4.17). For configuration I, unsteadiness effects are too important during the oscillation regime (*a*) identified above for the estimates (4.16) and (4.17) to be reliable. For this flow, oscillation pseudo-frequencies are higher than, or close to, the acoustic frequencies, thus indicating that compressibility effects and acoustic waves prevail over the actions of upstream vorticity/entropy perturbations and rocket-effect stabilization. This situation which predominates in this case, lasts only for the first few oscillations of the ablation front in configuration II, giving way, for increasing $\varkappa_\perp$, to a regime dominated by vorticity/entropy fluctuations.

The above results, once transcribed in terms of ablation-front distortions by means of (4.8), here equivalently

$$\widehat{X}_{abl}(k_\perp, t) = t^{4/3}\, \widehat{\mathscr{X}}_{abl}(\varkappa_\perp) = \frac{\varkappa_\perp}{k_\perp}\, \widehat{\mathscr{X}}_{abl}(\varkappa_\perp), \tag{4.18}$$

with

$$\widehat{\mathscr{X}}_{abl}(\varkappa_\perp) = -\frac{L_{abl}}{\bar{G}_{abl}}\, \widehat{\mathscr{G}}_{abl}(\varkappa_\perp), \tag{4.19}$$

or by means of front relative distortions

$$k_\perp\, \widehat{X}_{abl}(k_\perp, t) = \varkappa_\perp\, \widehat{\mathscr{X}}_{abl}(\varkappa_\perp), \tag{4.20}$$

establish the existence of three distinct regimes.

(i) *Algebraic growth.* For $k_\perp \ell_{con} \lesssim 0.1$, as a mere consequence of (4.12), (4.18) and (4.19), the front distortion amplitude is found to grow as

$$\widehat{X}_{abl}(k_\perp, t) \sim \mathrm{const}\, t^{4/3}, \tag{4.21}$$

as testified to by the relative distortion response growth (figure 8)

$$k_\perp\, \widehat{X}_{abl}(k_\perp, t) \sim \mathrm{const}\, \varkappa_\perp,$$

where the constant is bounded from above, in magnitude, by $|\widehat{\mathscr{X}}_{abl}(0)|$. This algebraic growth is a transcription, at the ablation front location, of the perturbation dynamics being dominated by the mean flow self-similarity, and, more specifically, by its unsteadiness – cf. (4.13) – and stretching – exemplified by the factor $t^{4/3}$ in (4.21). Through this dominance, the perturbation flow also inherits the physical characteristics of the mean flow, and particularly its confinement and compressibility.

(ii) *Modulated amplitude oscillations.* For $k_\perp \ell_{con} > 1$ but $\ell_{abl}/\lambda_\perp \ll 1$, an oscillatory regime of modulated amplitudes prevails (figure 8) during which the maximum front distortion amplitude is reached after one (for $k_\perp \ell_{con} \simeq 5$ in configuration I, cf. figure 8*a*) or several phase reversals (for $k_\perp \ell_{con} \simeq 50$ in configuration II, cf. figure 8*b*), this maximum being such that

$$\max_t |\widehat{X}_{abl}(k_\perp, t)| \propto k_\perp^{-1}, \tag{4.22}$$

by virtue of (4.20). The existence of such oscillatory behaviours is in agreement with simulations and modelling of laser imprinting (cf. § 4.1). However, a major qualitative difference with modellings which ignore the mean flow time-dependence, is the actual

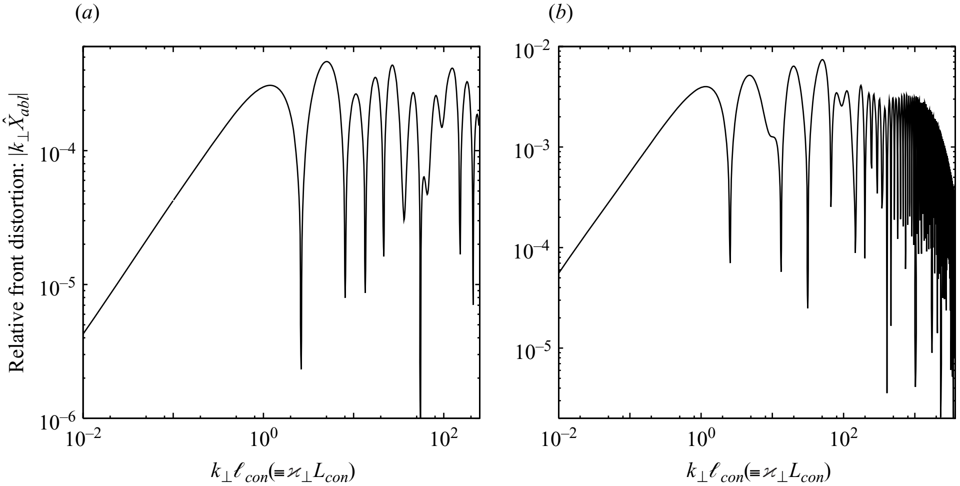

FIGURE 8. Reduced responses of configurations I and II of table 2 over the reduced wavenumber ranges of table 3. Relative ablation-front distortions, $k_\perp \widehat{X}_{abl}$, *vs.* the relative conduction zone thickness, $k_\perp \ell_{con}$, for configurations (*a*) I and (*b*) II. These front relative distortions which relate distortion amplitudes to perturbation wavelengths, depend solely on the reduced wavenumber $\varkappa_\perp$ – see (4.20) – and therefore entirely determine the temporal and spectral responses of the ablation fronts for all non-zero wavenumbers through a mere application of (4.18). The regimes of front distortion growth for $k_\perp \ell_{con} < 1$ – algebraic in $t^{4/3}$, i.e. linear in $\varkappa_\perp$, for $k_\perp \ell_{con} \lesssim 0.1$ – and of modulated amplitude oscillations for $k_\perp \ell_{con} > 1$ but $\ell_{abl}/\lambda_\perp \ll 1$, are apparent. (*b*) Exemplifies the damped oscillatory regime prevailing for $k_\perp \ell_{con} \gg 1$ with the behaviour of (4.23) as $\ell_{abl}/\lambda_\perp \to 1^-$.

occurrence of amplitude modulation – including some further amplification – in place of a predicted dominant decay. This difference is symbolized by the $t^{4/3}$ factor in (4.18) which results from the mean-flow stretching, and which has no possible equivalent in front-distortion descriptions with such modellings (see Goncharov *et al.* 2000, equation 9; 2006, equation 49). These modulated-amplitude front-distortion oscillations also result from the strong coupling of the ablation layer and shock-front dynamics, with a predominant or perceptible influence of the perturbation flow compressibility – including acoustic effects – and a decreasing effect of the mean flow unsteadiness. As the reduced wavenumber and the relative distance between the ablation layer and the shock front increase, the front distortion dynamics gradually evolves from a regime where compressibility and acoustic effects are dominating, to one being primarily influenced by the upstream vorticity/entropy perturbations left behind the fore-running shock.

(iii) *Damped oscillations.* For $k_\perp \ell_{con} \gg 1$ and $\ell_{abl}/\lambda_\perp \leqslant 1$, front distortion amplitudes follow a damped oscillatory regime, of limiting behaviour, as $\ell_{abl}/\lambda_\perp \to 1^-$,

$$\widehat{X}_{abl}(k_\perp, t) \sim t^{4/3}\, \mathrm{Re}\left\{b_0 \exp[(-\sigma + \mathrm{i}\omega) k_\perp t^{4/3}]\right\}, \tag{4.23}$$

with b_0 a complex constant, σ and ω real positive constants inherited from (4.15), (4.18), (4.19) – or equivalently

$$k_\perp\, \widehat{X}_{abl}(k_\perp, t) \sim \varkappa_\perp\, \mathrm{Re}\left\{b_0 \exp[(-\sigma + \mathrm{i}\omega)\varkappa_\perp]\right\},$$

(see figure 8*b*). During this regime, front-distortion decaying oscillations occur at frequencies sufficiently close to those characterizing vorticity/entropy-type oscillations (4.16), so that these may be held as descriptive of most of the front distortion dynamics.

This assertion is substantiated by the fact that the oscillation exponential damping rate, of which σ in (4.23) is an upper bound, is smaller – by more than one order of magnitude – than that given for the rocket-effect stabilization (Sanz 1996; Piriz *et al.* 1997). The form of the damping factor and the particularly high wavenumber values corresponding to this regime, for which no other results are currently available, call for further analyses that we leave for future studies. The fact that the oscillation frequencies are three times lower than the acoustic frequencies $c_S k_\perp$, leads to the conclusion that shock-induced acoustic waves are of a lesser influence, but also that compressibility effects should not be neglected.

Ablation front responses are further characterized by instantaneous front-distortion spectra, which, for the sake of a comparison between self-similar configurations, are presently taken at some physically equivalent time. Upon taking this time to correspond, in each configuration, to the penetration at the same dimensional depth, say Δ', of the shock wave front, we have, with the notations of (2.8), (B 3),

$$x_c t_\Delta^\alpha \bar{W} = \Delta',$$

where t_Δ denotes the corresponding dimensionless time. This definition and the relation

$$k_\perp = x_c k'_\perp,$$

between dimensionless, $k_\perp$, and dimensional, $k'_\perp$, wavenumbers, lead to the expression of the dimensional front-distortion spectrum at the dimensional time $t'_\Delta = t_c t_\Delta$, namely

$$\begin{aligned}\widehat{X}'_{abl}(k'_\perp, t'_\Delta) = x_c \widehat{X}_{abl}(k_\perp, t_\Delta) = x_c t_\Delta^\alpha \widehat{\mathscr{X}}_{abl}\left(\varkappa_\perp = x_c k'_\perp t_\Delta^\alpha\right) \\ = \frac{\Delta'}{\bar{W}} \widehat{\mathscr{X}}_{abl}\left(\varkappa_\perp = \frac{\Delta'}{\bar{W}} k'_\perp\right).\end{aligned} \qquad (4.24)$$

Given that this expression is independent of the flow-dimensional characteristic values, the corresponding spectral data are representative of any of the flows belonging to a given self-similar configuration, whence the comparison shown in figure 9. As it could be expected from (4.24), these ablation-front distortion spectra present the same characteristics as the ablation-front density perturbation responses displayed in figure 7(a,b), including the dominance of long wavelengths for the present configurations. The fact that the maximum responses are obtained for $k_\perp = 0$, and that these very responses obey the mean flow similarity (4.10a,b,d,e), points out the determining influence of the mean flow continuous and unsteady character on the long-wavelength perturbation evolutions. The ablation-layer stratification, via its characteristic length L_{abl} in (4.8), and its stretching in time are responsible for the front-distortion growth (4.21). This influence is also perceivable at shorter wavelengths since front-distortion amplification is more pronounced for the configuration with the largest relative ablation layer characteristic length, L_{abl}/L_{tot}; cf. the modulated amplitude oscillatory regimes for $k_\perp \ell_{con} > 1$ in figures 8(a,b). This influence is global since the mean flow with the largest ablation layer characteristic length presents the largest front-distortion amplitudes: the amplitudes of the spectrum envelope for configuration II are larger than those of configuration I (see figure 9), in agreement with the fact that ${\ell'_{abl}}^{\mathrm{II}} > {\ell'_{abl}}^{\mathrm{I}}$.

4.6. *An assessment of ablation parameter effects on laser imprinting*

Self-similar ablative flow responses such as those obtained for configurations I and II may also be used to assess the influence of different mean flow parameter variations on

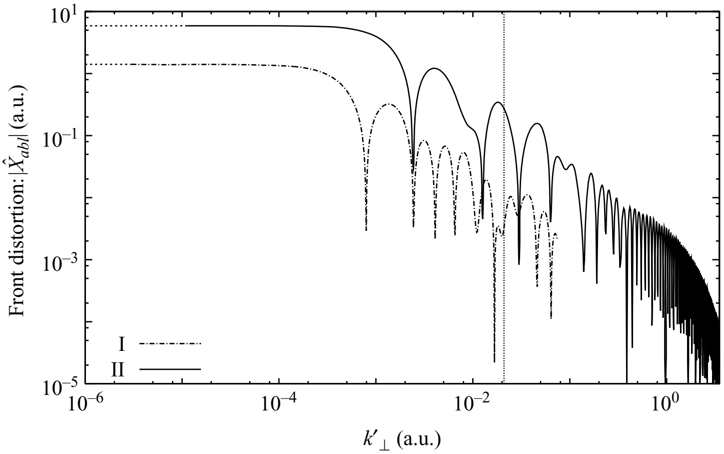

FIGURE 9. Reduced responses of configurations I and II of table 2 over the reduced wavenumber ranges of table 3. Comparison, between configurations I and II, of the instantaneous dimensional ablation-front distortion spectra, $\widehat{X}'_{abl}$, obtained by the time the shock-wave front, in each configuration, has reached the same penetration fluid depth Δ'; see (4.24). The dashed line portions of the spectral curves are joining, for each configuration, the $k'_{\perp} = \varkappa_{\perp min}\,\bar{W}/\Delta'$ data points to the respective results obtained for $k'_{\perp} = 0$. The thin vertical dotted line indicates the dimensional wavelength value, $\lambda'_{\perp}$, retained for carrying out the dimensional response comparisons of the flows listed in table 4; see §4.6. The above spectra are independent of the particular flows taken in each configuration, whence the axis scales in arbitrary units (a.u.).

the flow non-uniformity evolutions. A simple illustration is given here by considering, in addition to the two reference flows of configurations I and II, three distinct flows of the configuration II family (II a, II b, II c) differing from the configuration I reference flow through the sole variation of one of the following parameters:

(i) incident heat flux (II a);
(ii) external pressure (II b);
(iii) initial fluid density (II c).

The dimensional characteristic and reference values of the flows in table 4 are deduced from the definitions of the boundary conditions (2.7), boundary condition parameters (2.8) and reference values (2.9). Dimensional front-distortion comparisons between each of the configuration II flows and flow I demonstrate the following.

(i) An incident heat-flux, i.e. laser intensity, ramp steepening – $(\varphi_*^{(1)}/t_*)^{\mathrm{I}} > (\varphi_*^{(1)}/t_*)^{\mathrm{II\,a}}$ – induces a front distortion amplitude, growth regime duration and oscillation period decrease (see figure 10*a*). Note that in the case of laser imprinting by a constant irradiation, an increase of the incident laser intensity has been found, in simulations, to have a similar impact (see Goncharov *et al.* 2000).

(ii) A decrease of the external pressure – $(p_*/t_*^{2/3})^{\mathrm{I}} < (p_*/t_*^{2/3})^{\mathrm{II\,b}}$ – has identical consequences (see figure 10*b*).

(iii) A larger initial fluid density – $\rho_c^{\mathrm{I}} > \rho_c^{\mathrm{II\,c}}$ – leads to smaller front-distortion amplitudes but larger growth regime duration and oscillation periods (cf. figure 10*c*).

(iv) A more realistic description of the effects of an incident laser intensity increase, as that allowed by the comparison of flows I and II, suggests a more complex situation. For the present CH foil ablation, the fluid pressure and heat conductivity coefficient at the critical density surface also increase with the incident intensity (see table 4), so that the differences in front-distortion responses (figure 10*d*) result from a conjugation of

	Units	I	II	II a	II b	II c
t_*	10^{-9} s	4.8	*7.2*	36.94	12.0	36.94
ρ_c	$\mathrm{g\,cm^{-3}}$	1.04	1.04	1.04	1.04	$\mathit{3.76} \times \mathit{10}^{-3}$
R	$\mathrm{J\,g^{-1}\,K^{-1}}$	4.315	4.315	4.315	4.315	4.315
κ_0	$10^7\ \mathrm{W\,cm^{-1}\,K^{-1}}$	3.444	*7.180*	3.444	3.444	3.444
x_c	cm	0.192	0.339	0.532	0.304	8.852
v_c	$10^7\ \mathrm{cm\,s^{-1}}$	3.999	4.714	1.441	2.529	23.96
p_*	10^{11} Pa	1.663	*69.33*	6.482	*19.95*	6.482
T_c	10^7 K	3.706	5.150	0.4815	1.482	133.1
φ_*	$10^{14}\ \mathrm{W\,cm^{-2}}$	1.729	*28.0*	*0.8005*	4.323	13.31

TABLE 4. Dimensional characteristic and reference values for the original flows of configurations I and II of table 2, and their variants obtained from particular ablation physical parameter variations. The physical parameter values used for distinguishing the configuration II flows from that of configuration I are displayed in italics.

three effects. Hence, larger front-distortion amplitudes with comparable growth phase duration are observed for flow II (Abéguilé *et al.* 2006), suggesting an overcoming of the influence of the incident heat-flux rise (item (i) above) by that of an increased applied external pressure (item (ii)).

This kind of assessment of laser imprinting is of practical interest to ICF target design (e.g. see Metzler *et al.* 1999) and illustrates the wide variety of parametric studies that could be carried out by means of the present self-similar ablative flow family.

4.7. *Discussion*

As previously noted (§ 4.4), the present analysis of laser imprinting agrees, in trend, with previous results on the subject whether they be based on simulations, dedicated models or experiments. This analysis is performed for two particular self-similar configurations representing the compressible ablative flow, by electron heat conduction, of a semi-infinite slab of a monatomic gas initially at rest. These configurations rely on the single temperature approximation, the Spitzer–Härm conduction model, and assume that the critical surface of laser energy conversion into heat flux stays sufficiently close to the flow external boundary, so that the latter may be held to be the former, a peculiar situation in the context of ICF. The choice of a uniform state for the fluid initially at rest leads then to a flow similarity which is entirely determined, through a single exponent α of (2.12), by the temperature power ν entering the nonlinear heat conductivity expression (2.2). For the Spitzer–Härm conduction model ($\nu = 5/2$), this similarity which is defined by $\alpha = 4/3$, is bound to absorbed laser intensities increasing linearly with time. Stability results obtained within this particular framework are evidently restricted by these mean flow modelling limitations and by the specificity of the particular similarity which has been retained. Nevertheless some sufficiently general conclusions may be drawn from the present laser imprinting analysis in the light of previous findings on the subject.

Unsteadiness. Mean flow unsteadiness has been shown to be critical to the ablation front and flow perturbation evolutions for wavelengths ranging from being longer to being shorter than the conduction zone size. This is made patent not only by the dominance of the mean flow similarity at large wavelengths, but also by the dynamics of the front distortion oscillations beyond this regime at shorter wavelengths. Such an influential effect of the mean flow unsteadiness should be paralleled with

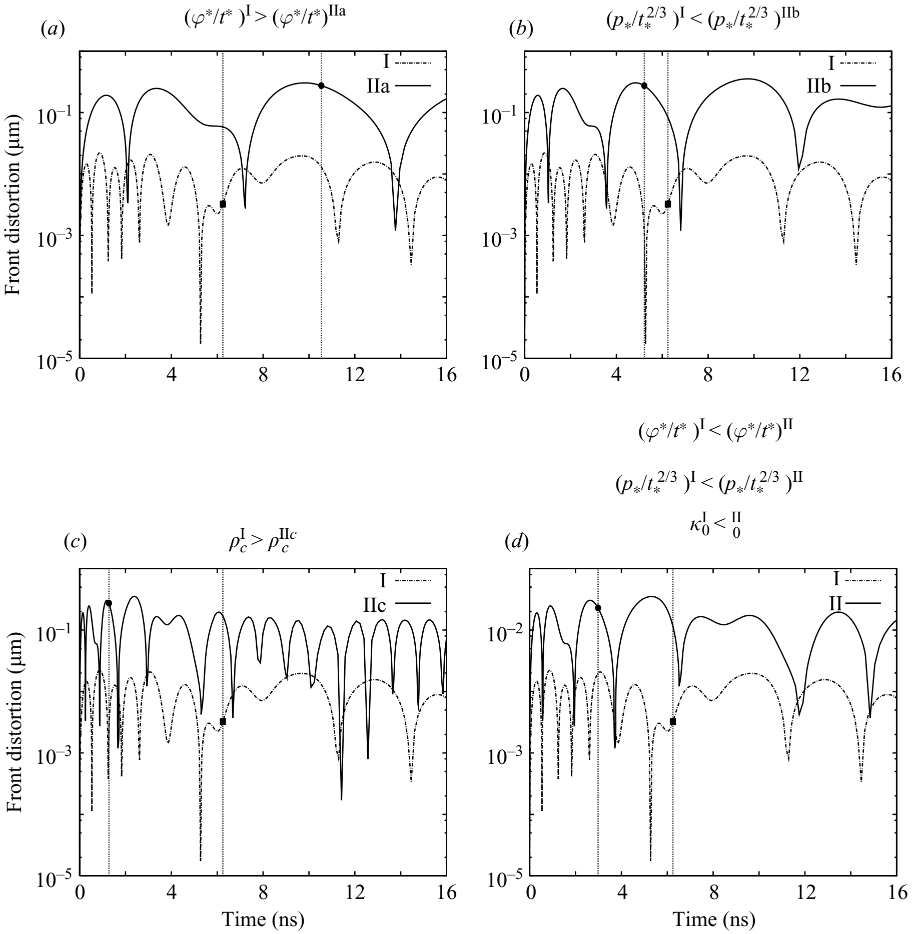

FIGURE 10. Comparisons of dimensional front-distortion temporal responses for the different flows in table 4 at a given laser intensity modulation wavelength $\lambda'_\perp = 300\,\mu$m. Effects of a variation of (*a*) laser intensity pulse ramp, (*b*) external pressure, (*c*) initial fluid density, and (*d*) of a conjugation of pulse ramp, external pressure and heat-conduction coefficient variations at the critical density surface, as resulting from a pulse ramp steepening in the simulation of a CH planar foil ablation. The thin vertical dotted lines indicate, for each flow, the times (■ for flow I, • for the flow II variants) of shock wave penetration at a fluid depth $\Delta' = 300\,\mu$m which correspond to the front-distortion spectra shown in figure 9.

numerical simulations of realistic laser imprint configurations (Emery *et al.* 1991; Velikovich *et al.* 1998; Goncharov *et al.* 2000, 2006) which have pointed out the time dependence, often linear, of the ablation-layer characteristic length, if not the self-similar character of the mean flow profiles (Velikovich *et al.* 1998), and the approximately linear-in-time growth of long-wavelength perturbations. In fact, in the few cases where sufficient data are available, regimes of perturbation initial growth and early oscillations, for which the perturbation evolution characteristic time exceeds that of the mean flow, may be identified for wavelengths sufficiently large, but which may be smaller than the conduction zone extent. This importance of the mean flow unsteadiness which is a feature common to both our particular flow model and to simulations of actual ICF-pellet early-time ablation, establishes the necessity of a temporal approach, as performed here, in stability studies at long to moderate wavelengths (here $k_\perp \ell_{con} \lesssim 100$). It also emphasizes the irrelevance, for these regimes, of any stability analysis relying on quasi-steady mean flow arguments. Such an analysis performed by Sanz *et al.* (2006) for weakly accelerated ablation front and which does not suffer the restrictions of ablation front discontinuous modellings, has nevertheless been claimed to be relevant to the early shell-irradiation stage. Therein a transition from Darrieus–Landau unstable modes to weakly damped oscillatory modes, as the perturbation wavelength decreases and crosses a marginal cutoff wavelength of the order of the conduction zone thickness, is presented as possibly describing the front distortion growth and damped oscillatory regimes found in laser imprinting. However, this marginal cutoff wavenumber crossing is inappropriate for describing perturbation evolutions in the unsteady early shell-irradiation flows. Indeed, as the instability growth rate vanishes across such a cutoff wavenumber, perturbation evolution times become much larger than the finite mean flow characteristic times, thus violating the quasi-steady mean flow assumption this analysis relies on.

Confinement. Flow confinement appears as another determining element in the ablation layer stability, not only, as is already known, for long wavelengths, but also for wavelengths shorter than the shocked-fluid region: vorticity/entropy fluctuations left out by the bounding shock wave are seen to dominate the ablation front distortion oscillations at sufficiently short wavelengths. A similar behaviour has also been noticed in results obtained with the early-time perturbation evolution model for quasi-steady ablation flows (Goncharov *et al.* 2006, figure 8). This significant flow-confinement effect illustrates the inadequacy of stability analyses of weakly accelerated ablation fronts in unbounded flows for describing perturbation evolutions during the early shell-irradiation stage.

Compressibility. An additional noticeable feature which comes out from the present perturbation flow responses is the finite compressibility of the ablation front perturbation evolution, as indicated by the ratios of perturbation evolution characteristic times over acoustic transit times. This compressibility which is, at long wavelengths, inherited from the mean-flow similarity dominance, is not becoming sufficiently small at shorter wavelengths to be reasonably neglected. Mean flow compressibility is also playing a particular role in the two specific configurations which have been considered here, in that, in each case, a part of the conduction zone expansion is supersonic. As a consequence, the thickening of the conduction zones is sufficiently high to inhibit the growth of perturbations due to the Darrieus–Landau instability (Landau & Lifshitz 1987). Indeed, as analysed in (Piriz & Portugues 2003) and illustrated by simulations (e.g. see Goncharov *et al.* 2006, figure 19), the occurrence of the Darrieus–Landau instability in ICF ablative flows is conditioned to a moderate expansion of the conduction zone. Let us note that a suitable choice of the self-similar mean flow boundary condition parameters ($\mathscr{B}_p$, $\mathscr{B}_\varphi$) can yield a totally different picture with respect to the conduction zone expansion (see Boudesocque-Dubois *et al.* 2008) and, possibly, to the presence of Darrieus–Landau unstable modes.

Stretching. Finally, the destabilizing effect of the mean flow stretching is pointed out as having a significant influence on the ablation front distortion dynamics. This influence is primarily identified from the difference in the qualitative description of the front distortion evolution between the present temporal stability results and those of the early-time perturbation evolution model for quasi-steady ablative flows (Goncharov *et al.* 2000, 2006). The latter predicts two regimes – amplitude growth and decaying oscillations – whereas from the former, three regimes are identified (Abéguilé *et al.* 2006) – amplitude growth, modulated amplitude oscillations, and damped oscillations. This qualitative difference is here evidenced in the specific case of the mean flow similarity of § 2 for the similarity exponent value $\alpha = 4/3$, and the incident heat-flux perturbation (4.4) with $\tau = 0$. Arguments may be developed in favour of a certain degree of generality regarding this mean flow stretching influence, based on the details of our ablation-front perturbation results. We should, however, keep in mind, when going into more detail, that the different perturbation evolution scaling laws exhibited in the present cases must be primarily taken as particular examples of behaviours which may occur in compressible unsteady ablative flows of ICF. For example, a change of the incident heat-flux perturbation temporal law would yield different time dependencies for the ablation front density perturbation and distortion (cf. Appendix A and (A 4)).

The present analysis which does not assume any particular scaling of the perturbation wavelength with respect to any of the flow characteristic lengths – contrary to models based on a sharp boundary ablation layer approximation – shows a maximum linear instability of the chosen flows at $k_\perp = 0$. We note that such a trend had been previously noticed in simulations of realistic constant irradiation imprinting configurations (Taylor *et al.* 1996; Nishihara *et al.* 1998; Schmitt *et al.* 2001), but never clearly established. In the present cases, this maximum instability corresponds to the difference between the mean flow and another similarity solution of the same family which results from the stipulated change in the slope of the laser intensity pulse ramp. The corresponding linear perturbations which are found to follow the mean flow similarity, are a mere confirmation of the linear stability of the chosen self-similar solutions with respect to one-dimensional perturbations. The fact that, for finite wavelengths exceeding the conduction zone thickness (i.e. for $0 < k_\perp \ell_{con} < 1$), the perturbation dynamics is dominated by the mean flow similarity, is due to the absence, at long wavelengths, of any stronger destabilizing multidimensional mechanism for the chosen flows (cf. the above discussion about the Darrieus–Landau instability), rather than to a predictable consequence of the flow model limitations (§ 4.1), in particular to the peculiar approximation of a material critical surface. The front distortion evolution – here at leading order in $t^{4/3}$ – is then inherent to this mean-flow similarity dominance and, in its detail, to the time-depencency law for lengths – the mean flow stretching – which characterizes the similarity. Other types of self-similar mean flows, provided that they be linearly stable with respect to one-dimensional perturbations, may equally display such a dominance of their linear multidimensional perturbation dynamics by the background similarity. This could be the case of the more realistic description of ablated ICF plasmas studied in Anisimov (1970) and Sanmartín & Barrero (1978*a*) which does not suffer from the material critical surface approximation of the present mean flow model.

For decreasing wavelengths ranging from being smaller than the conduction zone size ($k_\perp \ell_{con} > 1$) to being comparable to the shocked-fluid region extent ($k_\perp(\ell_{tot} - \ell_{con}) \simeq 1$, equivalently here $k_\perp \ell_{con} \simeq 250$), front distortions undergo modulated amplitude oscillations, including some further amplitude growth past the long-wavelength growth phase. During this regime, perturbation decoupling between the flow external boundary and the ablation front, here enhanced by the conduction zone supersonic expansions, is effective so that the front perturbation dynamics is at first approximation solely interfering with the nearby shock front. Constructive or destructive perturbation interactions between the shock front and ablation layer which may then occur, could be at the origin of the noticeable differences between the front-distortion modulated oscillations in the present flows (see figure 8) – a fact to be investigated in future studies. Amplitude growth which is probably here affected by compressibility effects, does not appear to originate from such effects: growth is present in both configurations, whereas the respective weights of these effects significantly differ at this stage. The occurrence of amplitude modulation and growth as it happens here, is ruled out by the early-time perturbation model for quasi-steady ablative flows which instead predicts decaying amplitude oscillations. Incorporating, in a somewhat *ad hoc* manner, the time dependence of the ablation-layer scale length in this model, introduces the possibility of some amplitude growth (Goncharov *et al.* 2006, § III.C). This mean-flow stretching effect which is thereby taken into account locally, is in the self-similar flow case a global effect, as summarized by the equivalent form of (4.18) valid at any flow location. Both approaches agree, however, in concluding that the influence of this stretching is destabilizing. Such a destabilization, which may have important implications in experiments since flow non-uniformities may be further amplified past the initial growth phase, induces a shift towards smaller wavelengths at the onset of front-distortion damping as compared to model predictions assuming a quasi-steady mean flow.

5. Conclusion

We have presented a physically and numerically consistent approach for studying the linear stability of self-similar ablative flows found in ICF, hereby accounting for mean flow unsteadiness, compressibility and stratification. This approach, which has no equivalent in the field, opens the prospect for future temporal stability analyses of a wide range of ICF ablative flows. The interest and necessity of such an approach is demonstrated through a study of the problem of laser imprinting in ICF, i.e. the response of a laser-driven ablative heat wave to illumination asymmetries.

The accuracy granted by the chosen numerical method has enabled us to obtain, with unprecedented detail, laser-imprint linear responses for wavelengths much larger than the flow extent down to wavelengths comparable to the ablation-front characteristic length. Conclusions drawn from these results are firmly established by the possibility of exploring such a wide perturbation spectrum and of obtaining flow responses in terms of reduced independent variables. These responses should be primarily viewed as particular examples of stability results which may be encountered in unsteady compressible ablative heat waves. In the two particular cases considered here, maximum linear instability is evidenced for illumination asymmetries of zero transverse wavenumber, that is for a modification of the sole incident laser intensity pulse ramp. The corresponding perturbations obeying the mean flow similarity, the dominant instability at long wavelengths is thus ruled by the mean flow characteristics, i.e. unsteadiness, compressibility and stretching. The existence and qualitative features of three distinct front distortion evolution regimes – algebraic growth, modulated amplitude oscillations and damped oscillations – as opposed to the two regimes – linear growth and damped oscillations – predicted by existing quasi-steady discontinuous and quasi-incompressible ablation models point out the inadequacy of such restrictive assumptions when considering the early shell-irradiation stage of an ICF pellet. This inadequacy is patent in the identified destabilizing effect of the mean flow stretching over a wide range of the wavenumber spectrum, and the strong influence of unsteadiness and compressibility at long wavelengths, aspects which are absent from these models. Another aspect covered by the present results is the existence of perturbation interactions between the different flow regions which is supported by the accurate description of perturbation evolutions throughout the flow. Accurate descriptions of these interactions are most needed in ICF, in particular for testing the reliability of hydrodynamics code simulations. The contribution of these interactions to the flow stability calls for a further analysis which is underway (Lombard *et al.* 2007).

Other mean flow or perturbation configurations could equally be treated with the present approach. In particular, we could investigate the influence of the flow compressibility or confinement – the latter in relation to an eventual Darrieus–Landau instability – on the flow stability in conjunction with unsteadiness and stratification effects. Other types of heat conduction, through proper choices of the heat conduction coefficient exponents (μ, ν), could be treated. More specifically, exponent values relevant to the ablation of low-atomic-number fluids by radiation would be worth considering since the present similarity flow structure exactly matches that of a radiation-driven ablative heat wave. In any case, given the high accuracy of computed perturbation results, such data should be profitable for benchmarking and improving hydrodynamics codes dedicated to ICF flow simulations.

In a broader prospect, stability results obtained with the present approach could furnish useful guidelines for further studies, whether they be theoretical, computational or experimental.

The authors wish to thank Professor J. Sanz (University Politécnica Madrid) for his suggestion of a possible perturbation dependent-variable reduction.

Appendix A. Mean flow and linear perturbation reduced equations

Here, we proceed to establish the variable transformations which lead to a reduced formulation of both (2.1), (2.2), (2.4), (2.5) for the mean flow, and (3.2*a*), (3.2*b*), (3.2*d*), (3.3), (3.4), (3.5) for the linear perturbations. In doing so, we recover, for the mean flow, the results of Brun *et al.* (1977) and Saillard (cf. Abéguilé *et al.* 2006), whereas the reduction of the linear perturbations has never been, to our knowledge, previously established. (The different systems of independent variables and the associated dependent variable notations used in this Appendix are summarized in table 5.)

Let us consider a similarity transformation of the form

$$q \longrightarrow \Lambda^{E_q}\, q, \tag{A 1}$$

where q denotes any of the 18 variables t, m, y, z, $\bar{\rho}$, $\bar{v}_x$, $\bar{T}$, $\bar{p}$, $\bar{\varphi}_x$, $\rho^{(1)}$, $(v_a^{(1)})_{a=x,y,z}$, $T^{(1)}$, $p^{(1)}$, $(\varphi_a^{(1)})_{a=x,y,z}$, and Λ is an arbitrary constant. Requiring this transformation to leave the set of equations (2.1), (2.2), (2.4), (2.5), (3.2*a*), (3.2*b*), (3.2*d*), (3.3), (3.4) and (3.5) unchanged, imposes that the 18 exponents E_t, E_m, $\ldots$, E_{φ_z} satisfy a system of 15 equations whose solutions may be expressed in terms of three parameters, here taken to be

$$\alpha = \frac{(2\nu-1)\,E_{\bar{v}_x} - \mu\,E_{\bar{\rho}}}{2(\nu-1)\,E_{\bar{v}_x} - (\mu+1)\,E_{\bar{\rho}}}, \quad \beta = \frac{(2\nu-1)\,E_{\bar{v}_x} - (\mu+1)\,E_{\bar{\rho}}}{2(\nu-1)\,E_{\bar{v}_x} - (\mu+1)\,E_{\bar{\rho}}}, \quad \delta = \frac{E_{v_x^{(1)}}}{E_{\bar{v}_x}}. \tag{A 2}$$

This transformation amounts then to considering the new independent variables

$$\xi = m\,t^{-\alpha}, \quad \eta = y\,t^{-\beta}, \quad \zeta = z\,t^{-\beta}, \tag{A 3}$$

along with dependent-variable reduced functions – say $\bar{\mathscr{G}}$, $\bar{\mathscr{V}}$, $\bar{\mathscr{T}}$, $\bar{\mathscr{P}}$, $\bar{\mathscr{F}}$ for the mean flow, and $\mathscr{G}$, $(\mathscr{V}_a)_{a=x,y,z}$, $\mathscr{T}$, $\mathscr{P}$, $(\mathscr{F}_a)_{a=x,y,z}$ for linear perturbations (cf. table 5)

	Arbitrary flow	Mean flow		Linear perturbations		Linear perturbation Fourier modes	
			reduced form		reduced form		reduced form
Independent variables	(x, y, z, t)	(m, t)	ξ	(m, y, z, t)	(ξ, η, ζ)	$(\xi, k_\perp, t)$	$(\xi, \varkappa_\perp)$
Quantity	q	$\bar{q}$	$\bar{Q}$, $\bar{\mathscr{Q}}$	$q^{(1)}$	$\mathscr{Q}$	$\widehat{Q}$	$\widehat{\mathscr{Q}}$
Density	ρ	$\bar{\rho}$	$\bar{G}$, $\bar{\mathscr{G}}$	$\rho^{(1)}$	$\mathscr{G}$	$\widehat{G}$	$\widehat{\mathscr{G}}$
x velocity	v_x	$\bar{v}_x$	$\bar{V}$, $\bar{\mathscr{V}}$	$v_x^{(1)}$	$\mathscr{V}_x$	$\widehat{V}_x$	$\widehat{\mathscr{V}}_x$
Transverse expansion	–	–	–	$\nabla_\perp \cdot \boldsymbol{v}_\perp^{(1)}$	$\nabla_{(\eta,\zeta)} \cdot \mathscr{V}_\perp$	$\widehat{D}_\perp$	$\widehat{\mathscr{D}}_\perp$
Pressure	p	$\bar{p}$	$\bar{P}$, $\bar{\mathscr{P}}$	$p^{(1)}$	$\mathscr{P}$	$\widehat{P}$	$\widehat{\mathscr{P}}$
Temperature	T	$\bar{T}$	$\bar{\Theta}$, $\bar{\mathscr{T}}$	$T^{(1)}$	$\mathscr{T}$	$\widehat{\Theta}$	$\widehat{\mathscr{T}}$
x heat flux	φ_x	$\bar{\varphi}_x$	$\bar{\Phi}$, $\bar{\mathscr{F}}$	$\varphi_x^{(1)}$	$\mathscr{F}_x$	$\widehat{\Phi}_x$	$\widehat{\mathscr{F}}_x$
Transverse heat flux	–	–	–	$\boldsymbol{\varphi}_\perp^{(1)}$	$\mathscr{F}_\perp$	–	–
Surface deformation	x_Γ	–	–	$x_\Gamma^{(1)}$	$\mathscr{X}_\Gamma$	$\widehat{X}_\Gamma$	$\widehat{\mathscr{X}}_\Gamma$
Shock front x velocity	w_x	$\bar{w}_x$	$\bar{W}$, $\bar{\mathscr{W}}$	$w_x^{(1)}$	$\mathscr{W}$	$\hat{\dot{X}}_s$	$\widehat{\mathscr{W}}$
Shock front relative x velocity	u_x	$\bar{u}_x$	$\bar{U}$, $\bar{\mathscr{U}}$	$u_x^{(1)}$	–	–	–

TABLE 5. Recapitulation of the different systems of independent variables and of the corresponding dependent variable notations used throughout the paper.

– obeying the relations

$$\left.\begin{aligned}
\bar{\rho}(m,t) &= t^{\alpha-\beta}\,\bar{\mathscr{G}}(\xi), & \rho^{(1)}(m,y,z,t) &= t^{\alpha-\beta+(\delta-1)(\beta-1)}\,\mathscr{G}(\xi,\eta,\zeta),\\
\bar{v}_x(m,t) &= t^{\beta-1}\,\bar{\mathscr{V}}(\xi), & v_a^{(1)}(m,y,z,t) &= t^{\delta(\beta-1)}\,\mathscr{V}_a(\xi,\eta,\zeta),\ a=x,y,z,\\
\bar{T}(m,t) &= t^{2(\beta-1)}\,\bar{\mathscr{T}}(\xi), & T^{(1)}(m,y,z,t) &= t^{(\delta+1)(\beta-1)}\,\mathscr{T}(\xi,\eta,\zeta),\\
\bar{p}(m,t) &= t^{\alpha-\beta+2(\beta-1)}\,\bar{\mathscr{P}}(\xi), & p^{(1)}(m,y,z,t) &= t^{\alpha-\beta+(\delta+1)(\beta-1)}\,\mathscr{P}(\xi,\eta,\zeta),\\
\bar{\varphi}_x(m,t) &= t^{\alpha-\beta+3(\beta-1)}\,\bar{\mathscr{F}}(\xi), & \varphi_a^{(1)}(m,y,z,t) &= t^{\alpha-\beta+(\delta+2)(\beta-1)}\,\mathscr{F}_a(\xi,\eta,\zeta),\\
& & & \qquad a=x,y,z.
\end{aligned}\right\} \tag{A 4}$$

Inserting (A 3) and (A 4) into (2.5) yields the system of first-order ODEs

$$\left.\begin{aligned}
&\mathrm{d}_\xi\left(\frac{\alpha\xi}{\bar{\mathscr{G}}}+\bar{\mathscr{V}}\right)=\frac{\beta}{\bar{\mathscr{G}}},\\
&\mathrm{d}_\xi(\alpha\xi\bar{\mathscr{V}}-\bar{\mathscr{P}})=(\alpha+\beta-1)\,\bar{\mathscr{V}},\\
&\mathrm{d}_\xi\left(\alpha\xi\left[\frac{\bar{\mathscr{V}}^2}{2}+\frac{\bar{\mathscr{T}}}{\gamma-1}\right]-\bar{\mathscr{P}}\bar{\mathscr{V}}-\bar{\mathscr{F}}\right)=[\alpha+2(\beta-1)]\left(\frac{\bar{\mathscr{V}}^2}{2}+\frac{\bar{\mathscr{T}}}{\gamma-1}\right),\\
&\mathrm{d}_\xi\bar{\mathscr{T}}=-\bar{\mathscr{G}}^{\mu-1}\bar{\mathscr{T}}^{-\nu}\bar{\mathscr{F}},
\end{aligned}\right\} \tag{A 5}$$

with

$$\bar{\mathscr{P}}=\bar{\mathscr{G}}\,\bar{\mathscr{T}}, \tag{A 6}$$

while the linear perturbation equations (3.2*a*), (3.2*b*), (3.2*d*), (3.3), (3.4) and (3.5) are replaced by the system of PDEs

$$\left.\begin{aligned}
&[(\delta-1)(\beta-1)-\alpha\xi\partial_\xi-\beta\partial_{\boldsymbol{\eta}}](\mathscr{G}/\bar{\mathscr{G}})+\partial_\xi(\bar{\mathscr{G}}\mathscr{V}_x)+\nabla_{(\eta,\zeta)}\cdot\mathscr{V}_\perp=0,\\
&[\delta(\beta-1)-\alpha\xi\partial_\xi-\beta\partial_{\boldsymbol{\eta}}]\mathscr{V}_x+\bar{\mathscr{G}}\,\mathrm{d}_\xi\bar{\mathscr{V}}\,\mathscr{V}_x+\partial_\xi\mathscr{P}-\mathrm{d}_\xi\bar{\mathscr{P}}\,\mathscr{G}/\bar{\mathscr{G}}=0,\\
&[\delta(\beta-1)-\alpha\xi\partial_\xi-\beta\partial_{\boldsymbol{\eta}}]\nabla_{(\eta,\zeta)}\cdot\mathscr{V}_\perp+\Delta_{(\eta,\zeta)}\mathscr{P}/\bar{\mathscr{G}}=0,\\
&[(\delta+1)(\beta-1)-\alpha\xi\partial_\xi-\beta\partial_{\boldsymbol{\eta}}]\mathscr{T}+\bar{\mathscr{G}}\,\mathrm{d}_\xi\bar{\mathscr{T}}\,\mathscr{V}_x+(\gamma-1)(\bar{\mathscr{G}}\,\mathrm{d}_\xi\bar{\mathscr{V}}\,\mathscr{T}\\
&\quad+\bar{\mathscr{P}}\,\partial_\xi\mathscr{V}_x+\partial_\xi\mathscr{F}_x-\mathrm{d}_\xi\bar{\mathscr{F}}\,\mathscr{G}/\bar{\mathscr{G}}+\bar{\mathscr{T}}\,\nabla_{(\eta,\zeta)}\cdot\mathscr{V}_\perp-\nabla_{(\eta,\zeta)}\cdot\mathscr{F}_\perp/\bar{\mathscr{G}})=0,
\end{aligned}\right\}\qquad\text{(A 7)}$$

with the notations $\boldsymbol{\eta}=\eta\boldsymbol{e}_y+\zeta\boldsymbol{e}_z$ and $\partial_{\boldsymbol{\eta}}\,.\;=\boldsymbol{\eta}\cdot\nabla_{(\eta,\zeta)}\,.$, and with the expressions

$$\mathscr{F}_x=-\bar{\mathscr{G}}^{1-\mu}\bar{\mathscr{T}}^{\nu}(\partial_\xi\mathscr{T}+\mathrm{d}_\xi\bar{\mathscr{T}}[(1-\mu)\mathscr{G}/\bar{\mathscr{G}}+\nu\mathscr{T}/\bar{\mathscr{T}}]),\qquad\text{(A 8a)}$$

$$\mathscr{F}_y=-\bar{\mathscr{G}}^{-\mu}\bar{\mathscr{T}}^{\nu}\partial_\eta\mathscr{T},\quad\mathscr{F}_z=-\bar{\mathscr{G}}^{-\mu}\bar{\mathscr{T}}^{\nu}\partial_\zeta\mathscr{T},\qquad\text{(A 8b)}$$

and

$$\mathscr{P}=\bar{\mathscr{G}}\mathscr{T}+\mathscr{G}\bar{\mathscr{T}}.\qquad\text{(A 9)}$$

In obtaining these equations, use has been made of the partial derivative transformations

$$\left.\begin{aligned}
&\partial_t q^{(1)}(m,y,z,t)=t^{n-1}[n-\alpha\xi\partial_\xi-\beta\partial_{\boldsymbol{\eta}}]\mathscr{Q}(\xi,\eta,\zeta),\\
&\partial_m q^{(1)}(m,y,z,t)=t^{n-\alpha}\partial_\xi\mathscr{Q}(\xi,\eta,\zeta),\\
&\partial_y q^{(1)}(m,y,z,t)=t^{n-\beta}\partial_\eta\mathscr{Q}(\xi,\eta,\zeta),\quad\partial_z q^{(1)}(m,y,z,t)=t^{n-\beta}\partial_\zeta\mathscr{Q}(\xi,\eta,\zeta),
\end{aligned}\right\}\qquad\text{(A 10)}$$

valid for any flow-dependent variable q such that $q^{(1)}(m,y,z,t)\equiv t^n\mathscr{Q}(\xi,\eta,\zeta)$.

A.1. *Compatibility conditions for self-similar mean flows*

The self-similar formulation (A 2)–(A 5) of the mean flow system of PDEs (2.5) is subject to certain constraints – compatibility conditions – bearing on that system initial and boundary conditions. Namely, compatible mean flow initial conditions must be such that

$$\left.\begin{aligned}
&\bar{\rho}(m,0)=C^I_{\bar{\rho}}\,m^{E_{\bar{\rho}}/E_m} &&\text{or}\quad \lim_{\xi\to+\infty}\xi^{-(\alpha-\beta)/\alpha}\,\bar{\mathscr{G}}(\xi)=C^I_{\bar{\rho}},\\
&\bar{v}_x(m,0)=C^I_{\bar{v}_x}\,m^{E_{\bar{v}_x}/E_m} &&\text{or}\quad \lim_{\xi\to+\infty}\xi^{-(\beta-1)/\alpha}\,\bar{\mathscr{V}}(\xi)=C^I_{\bar{v}_x},\\
&\bar{T}(m,0)=C^I_{\bar{T}}\,m^{E_{\bar{T}}/E_m} &&\text{or}\quad \lim_{\xi\to+\infty}\xi^{-2(\beta-1)/\alpha}\,\bar{\mathscr{T}}(\xi)=C^I_{\bar{T}},\\
&\bar{p}(m,0)=C^I_{\bar{p}}\,m^{E_{\bar{p}}/E_m} &&\text{or}\quad \lim_{\xi\to+\infty}\xi^{-[\alpha-\beta+2(\beta-1)]/\alpha}\,\bar{\mathscr{P}}(\xi)=C^I_{\bar{p}},\\
&\bar{\varphi}_x(m,0)=C^I_{\bar{\varphi}_x}\,m^{E_{\bar{\varphi}_x}/E_m} &&\text{or}\quad \lim_{\xi\to+\infty}\xi^{-[\alpha-\beta+3(\beta-1)]/\alpha}\,\bar{\mathscr{F}}(\xi)=C^I_{\bar{\varphi}_x},
\end{aligned}\right\}\qquad\text{(A 11)}$$

while boundary conditions at some particular point of Lagrangian abscissa $m=m_\Gamma(t)$, equivalently $\xi=\xi_\Gamma=m_\Gamma(t)\,t^{-\alpha}$, ought to be of the form

$$\bar{q}(m_\Gamma(t),t)=C^\Gamma_{\bar{q}}\,t^{E_{\bar{q}}/E_t}\quad\text{or}\quad\bar{\mathscr{Q}}(\xi_\Gamma)=C^\Gamma_{\bar{q}}.\qquad\text{(A 12)}$$

Let us note that the initial and boundary-conditions presently considered in this paper (see § 2) correspond to the particular choice

$$E_{\bar{\rho}}=0,\quad C^I_{\bar{\rho}}=1,\quad C^I_{\bar{v}_x}=0,\quad C^I_{\bar{T}}=0,\quad C^I_{\bar{p}}=0,\quad C^I_{\bar{\varphi}_x}=0,\qquad\text{(A 13)}$$

in (A 11), whence the definition

$$\alpha = \beta = \frac{2\mu - 1}{2(\mu - 1)}, \tag{A 14}$$

and, for (A 12) taken at the origin $\xi = 0$, to the boundary-condition parameter and exponent values

$$\left.\begin{aligned} C^{\Gamma}_{\bar{p}} = C^{\Gamma}_{\bar{\rho}}\, C^{\Gamma}_{\bar{T}} = \mathscr{B}_p, \quad C^{\Gamma}_{\bar{\varphi}_x} = \mathscr{B}_{\varphi}, \\ E_{\bar{p}}/E_t = E^{e}_{\bar{p}} = \alpha - \beta + 2(\beta - 1) = 2(\alpha - 1), \\ E_{\bar{\varphi}_x}/E_t = E^{e}_{\bar{\varphi}} = \alpha - \beta + 3(\beta - 1) = 3(\alpha - 1), \end{aligned}\right\} \tag{A 15}$$

the last two relations being imposed by (A 4). Hence, the generalized transformation (A 2)–(A 4) reduces to the similarity transformation of § 2.2, the corresponding reduced functions $\bar{\mathscr{G}}$, $\bar{\mathscr{V}}$, $\bar{\mathscr{T}}$, $\bar{\mathscr{P}}$, $\bar{\mathscr{F}}$ being merely the functions $\bar{G}$, $\bar{V}$, $\bar{\Theta}$, $\bar{P}$, $\bar{\Phi}$ of (2.11)–(2.19).

A.2. *Compatible initial and boundary conditions for reduced linear perturbation equations*

The facts that the reduced system (A 7) involves PDEs and that its non-trivial solutions do not appear to be separable (Boudesocque-Dubois 2000), considerably complicate the task of identifying linear perturbation initial conditions for (3.2*a*), (3.2*b*), (3.2*d*), (3.3), (3.4) and (3.5) that could be compatible with the transformation (A 2)–(A 4). Compatible boundary conditions are much more easily inferred. Provided that both the imposed density $\rho_e^{(1)}$ and incident heat flux $\varphi_{e_x}^{(1)}$ at the fluid external surface, and the fluid quantities upstream from the shock-wave front comply with (A 4), the boundary conditions at $\xi = 0$ and $\xi = \xi_s$ reduce to systems of PDEs in the (ξ, η, ζ) variables, namely,

$$\left.\begin{aligned} &\mathscr{G}|_{+} + (\bar{\mathscr{G}}\mathrm{d}_{\xi}\bar{\mathscr{G}})|_{+}\mathscr{X}_e = \mathscr{G}_e, \\ &\mathscr{F}_x|_{+} + (\bar{\mathscr{G}}\mathrm{d}_{\xi}\bar{\mathscr{F}})\big|_{+}\mathscr{X}_e = \mathscr{F}_{ex}, \\ &\mathscr{V}_x|_{+} + [(\bar{\mathscr{G}}\mathrm{d}_{\xi}\bar{\mathscr{V}})|_{+} - \delta(\beta - 1) - 1 + \beta\partial_{\eta}]\,\mathscr{X}_e = 0, \end{aligned}\right\} \tag{A 16}$$

at $\xi = 0$, and (B 6) at $\xi = \xi_s$, where, in agreement with the relation for the velocity linear perturbation reduced function in (A 4), the boundary surface linear deformations $x_e^{(1)}$ and $x_s^{(1)}$ satisfy the equation

$$x_{\Gamma}^{(1)}(y, z, t) = t^{\delta(\beta - 1) + 1}\,\mathscr{X}_{\Gamma}(\eta, \zeta). \tag{A 17}$$

A.3. *Linear perturbation reduced Fourier mode equations*

Considering the $\eta\zeta$-Fourier transform of (A 7) yields a system of PDEs in the variable $(\xi, \varkappa_\eta, \varkappa_\zeta)$ – where $\varkappa_\eta$ and $\varkappa_\zeta$ denote the $\eta\zeta$-Fourier space variables – which may be further simplified into a two-dimensional system of PDEs, once rewritten in the Fourier polar coordinates $(\varkappa_\perp, \theta)$ such that

$$\varkappa_\eta = \varkappa_\perp \cos\theta, \quad \varkappa_\zeta = \varkappa_\perp \sin\theta. \tag{A 18}$$

With the notation

$$\left.\begin{aligned} \widehat{\mathscr{G}}(\xi, \varkappa_\perp) &\equiv \mathfrak{F}_{\eta\zeta}[\mathscr{G}(\xi, \eta, \zeta)], & \widehat{\mathscr{V}}_x(\xi, \varkappa_\perp) &\equiv \mathfrak{F}_{\eta\zeta}[\mathscr{V}_x(\xi, \eta, \zeta)], \\ \widehat{\mathscr{D}}_\perp(\xi, \varkappa_\perp) &\equiv \mathfrak{F}_{\eta\zeta}[\nabla_{(\eta,\zeta)} \cdot \mathscr{V}_\perp(\xi, \eta, \zeta)], & \widehat{\mathscr{T}}(\xi, \varkappa_\perp) &\equiv \mathfrak{F}_{\eta\zeta}[\mathscr{T}(\xi, \eta, \zeta)], \\ \widehat{\mathscr{P}}(\xi, \varkappa_\perp) &\equiv \mathfrak{F}_{\eta\zeta}[\mathscr{P}(\xi, \eta, \zeta)], & \widehat{\mathscr{F}}_x(\xi, \varkappa_\perp) &\equiv \mathfrak{F}_{\eta\zeta}[\mathscr{F}_x(\xi, \eta, \zeta)], \end{aligned}\right\} \tag{A 19}$$

for the linear perturbation reduced function Fourier transforms, the relevant system of PDEs reads

$$\left.\begin{aligned}
&[(\delta-1)(\beta-1)-\alpha\xi\partial_\xi+\beta\mathbb{D}](\widehat{\mathscr{G}}/\bar{\mathscr{G}})+\partial_\xi(\bar{\mathscr{G}}\widehat{\mathscr{V}}_x)+\widehat{\mathscr{D}}_\perp=0,\\
&[\delta(\beta-1)-\alpha\xi\partial_\xi+\beta\mathbb{D}]\widehat{\mathscr{V}}_x+\bar{\mathscr{G}}\,\mathrm{d}_\xi\bar{\mathscr{V}}\,\widehat{\mathscr{V}}_x+\partial_\xi\widehat{\mathscr{P}}-\mathrm{d}_\xi\bar{\mathscr{P}}\,\widehat{\mathscr{G}}/\bar{\mathscr{G}}=0,\\
&[\delta(\beta-1)-\alpha\xi\partial_\xi+\beta\mathbb{D}]\widehat{\mathscr{D}}_\perp-\varkappa_\perp^2\widehat{\mathscr{P}}/\bar{\mathscr{G}}=0,\\
&[(\delta+1)(\beta-1)-\alpha\xi\partial_\xi+\beta\mathbb{D}]\widehat{\mathscr{T}}+\bar{\mathscr{G}}\,\mathrm{d}_\xi\bar{\mathscr{T}}\,\widehat{\mathscr{V}}_x+(\gamma-1)(\bar{\mathscr{G}}\,\mathrm{d}_\xi\bar{\mathscr{V}}\,\widehat{\mathscr{T}}\\
&\quad+\bar{\mathscr{P}}\,\partial_\xi\widehat{\mathscr{V}}_x+\partial_\xi\widehat{\mathscr{F}}_x-\mathrm{d}_\xi\bar{\mathscr{F}}\,\widehat{\mathscr{G}}/\bar{\mathscr{G}}+\bar{\mathscr{T}}\,\widehat{\mathscr{D}}_\perp-\varkappa_\perp^2\bar{\mathscr{G}}^{-\mu-1}\bar{\mathscr{T}}^{\nu}\widehat{\mathscr{T}})=0,
\end{aligned}\right\} \tag{A 20}$$

where $\mathbb{D}$ denotes the operator

$$\mathbb{D}.=\partial_{\varkappa_\perp}(\varkappa_\perp.)+1., \tag{A 21}$$

and where the expressions for $\widehat{\mathscr{F}}_x$ and $\widehat{\mathscr{P}}$ are deduced from (A 8) and (A 9) after an obvious change of notation. The proper boundary condition formulations along the fluid external surface $\xi=0$ and the shock-wave front $\xi=\xi_s$ follow immediately from (A 16) and (B 6), in effect

$$\left.\begin{aligned}
&\widehat{\mathscr{G}}|_+ +(\bar{\mathscr{G}}\mathrm{d}_\xi\bar{\mathscr{G}})|_+\widehat{\mathscr{X}}_e=\widehat{\mathscr{G}}_e,\\
&\widehat{\mathscr{F}}_x|_+ +(\bar{\mathscr{G}}\mathrm{d}_\xi\bar{\mathscr{F}})|_+\widehat{\mathscr{X}}_e=\widehat{\mathscr{F}}_{ex},\\
&\widehat{\mathscr{V}}_x|_+ +[(\bar{\mathscr{G}}\mathrm{d}_\xi\bar{\mathscr{V}})|_+-\delta(\beta-1)-1-\beta\mathbb{D}]\,\widehat{\mathscr{X}}_e=0,
\end{aligned}\right\} \tag{A 22}$$

for the former, and (B 7) for the latter, with the convention $\widehat{\mathscr{X}}_\Gamma(\varkappa_\perp)\equiv\mathfrak{F}_{\eta\zeta}[\mathscr{X}_\Gamma(\eta,\zeta)]$.

Since the Fourier polar angle θ does not explicitly appear in (A 20), (A 22) or (B 7) – whence justifying the notations of (A 19) – system (A 20) need only be considered for $(\xi,\varkappa_\perp)$ in $[0,\xi_s)\times[0,+\infty)$. Differences between solutions to this system for different angles θ may thus result only from differences in boundary values imposed at the flow boundaries $\xi=0$ and $\xi=\xi_s^+$, or along the wavenumber domain boundaries $\varkappa_\perp=0$ and $\varkappa_\perp\to+\infty$. Let us note, however, that (A 20) depends on the free parameter δ which determines the linear perturbation time power-laws that may be imposed along the flow boundaries. Further characterization of the mathematical properties of this system in terms of boundary condition specifications, existence or methods of solutions is beyond the scope of this paper. Nevertheless, the possibility of a linear perturbation description in terms of a reduced set of independent variables, as described by (A 4), (A 19), (A 20), can turn out to be especially valuable when analysing numerical integration results of the temporal PDE system (3.10). In particular we may take advantage of the relation which exists between the yz- and $\eta\zeta$-Fourier transforms of a given flow variable linear perturbation $q^{(1)}$, namely

$$\widehat{Q}(\xi,k_\perp,t)=t^{n+2\beta}\,\widehat{\mathscr{Q}}(\xi,t^\beta k_\perp), \tag{A 23}$$

provided that $q^{(1)}$ is such that $q^{(1)}(m,y,z,t)=t^n\,\mathscr{Q}(\xi,\eta,\zeta)$.

Note that the reduced Fourier transform equations and relation relevant to the self-similar flows of § 2.2, namely (3.18) and (3.19), simply arise as the particular case of (A 20) and (A 23) when (A 14) applies.

Appendix B. Rankine–Hugoniot relations at the shock-wave front

Linearly perturbed Rankine–Hugoniot relations have been derived in many instances (e.g. see Richtmyer 1960), although, most often in the absence of a heat flux and assuming uniform mean flows on both sides of the discontinuity. Here, having in mind the one-dimensional flows of § 2.2, we shall assume only that the upstream heat flux is vanishing and that the shock-front surface distortion comes as

$$x = x_s(y, z, t; \epsilon),$$

with the notation of § 3. The general form of the Rankine–Hugoniot jump relations at a shock-wave front, in the presence of a heat flux $\boldsymbol{\varphi}$ and in the absence of mass forces, may be written as (e.g. see Germain & Muller 1994)

$$\left.\begin{array}{l} [\rho u_a n_a]_D^U = 0, \\ [(\rho v_a u_b - p\delta_{ab})n_b]_D^U = 0, \quad \text{for } a = x, y, z, \\ \left[\left(\rho\left[\mathscr{E} + \tfrac{1}{2}v_b v_b\right]u_a - p v_a - \varphi_a\right)n_a\right]_D^U = 0, \end{array}\right\} \tag{B 1}$$

where $\boldsymbol{n}$ is the vector normal to the shock-wave front surface, and $\boldsymbol{u} = \boldsymbol{w} - \boldsymbol{v}$ is the shock front velocity relative to the fluid, $\boldsymbol{w}$ being the front velocity in the chosen frame of reference. In addition, downstream (respectively upstream) – with respect to the shock front – values of flow quantities are designated by the subscript D (subscript U), while subscripts a and b identify vector components in the Cartesian coordinate system, and δ_{ab} is the usual Kronecker symbol – Einstein's convention being used for repeated subscripts.

B.1. *Mean flow Rankine–Hugoniot relations in the self-similar variable*

Applying (B 1) to the one-dimensional self-similar flows of § 2.2, i.e. for an upstream state given by $(\bar{G}_U, \bar{V}_U, \bar{\Theta}_U) = (1, 0, 0)$, and assuming a discontinuity of the temperature, leads to the expressions

$$\bar{G}_D = \frac{(\gamma+1)\bar{W}^2}{\gamma\bar{W}^2 - \mathscr{R}}, \quad \bar{V}_D = \frac{\bar{W}^2 + \mathscr{R}}{\bar{W}\,(\gamma+1)}, \quad \bar{P}_D = \bar{W}\;\bar{V}_D, \tag{B 2}$$

with

$$\mathscr{R} = \sqrt{\bar{W}^4 - 2(\gamma-1)(\gamma+1)\bar{W}\bar{\Phi}_D},$$

where $\bar{W}$ is the self-similar shock-front reduced velocity, of expression

$$\bar{W} \equiv t^{1-\alpha}\,[\partial_t \bar{x}(m,t)]_\xi|_{\xi_s} = [\alpha\xi/\bar{G}(\xi) + \bar{V}(\xi)]|_{\xi_s}. \tag{B 3}$$

B.2. *Linear perturbation Rankine–Hugoniot relations*

The corresponding jump relations for the linear perturbations – expressed in terms of the transverse flow expansion, $\nabla_\perp \cdot \boldsymbol{v}_\perp^{(1)}$, and the Lagrangian coordinate m – come as

$$\left.\begin{array}{l} \left[\rho^{(1)}\bar{u}_x + \bar{\rho}u_x^{(1)} + \bar{\rho}x_s^{(1)}\,\partial_m(\bar{\rho}\bar{u}_x)\right]_D^U = 0, \\ \left[\bar{\rho}\bar{v}_x u_x^{(1)} + \bar{\rho}v_x^{(1)}\bar{u}_x + \rho^{(1)}\bar{v}_x\bar{u}_x - p^{(1)} + \bar{\rho}x_s^{(1)}\,\partial_m(\bar{\rho}\bar{v}_x\bar{u}_x - \bar{p})\right]_D^U = 0, \\ \left[\nabla_\perp \cdot \boldsymbol{v}_\perp^{(1)} + \bar{v}_x\Delta_\perp x_s^{(1)}\right]_D^U = 0, \\ \left[\left(\dfrac{p^{(1)}}{\gamma-1} + \rho^{(1)}\dfrac{\bar{v}_x^2}{2} + \bar{\rho}\bar{v}_x v_x^{(1)}\right)\bar{u}_x + \left(\dfrac{\bar{p}}{\gamma-1} + \bar{\rho}\dfrac{\bar{v}_x^2}{2}\right)u_x^{(1)} - \bar{p}v_x^{(1)} - p^{(1)}\bar{v}_x \right. \\ \quad \left. + \bar{\rho}x_s^{(1)}\,\partial_m\left(\left[\dfrac{\bar{p}}{\gamma-1} + \bar{\rho}\dfrac{\bar{v}_x^2}{2}\right]\bar{u}_x - \bar{p}\bar{v}_x\right)\right]_D^U + \varphi_x^{(1)}{}_D + \bar{\rho}_D x_s^{(1)}(\partial_m\bar{\varphi}_x)_D = 0, \end{array}\right\} \tag{B 4}$$

with $u_x^{(1)} = w_x^{(1)} - v_x^{(1)} = \dot{x}_s^{(1)} - v_x^{(1)}$, and the notation introduced in (3.2)–(3.8). These relations cover the classical case (Richtmyer 1960) of uniform downstream and upstream mean flows in the absence of heat conduction.

B.2.1. *Fourier mode Rankine–Hugoniot relations*

For a uniform upstream mean flow, as is the case for the self-similar flows of § 2, the jump relations for the linear perturbation *yz*-Fourier component vector $\widehat{\boldsymbol{Z}} = (\widehat{G}, \widehat{V}_x, \widehat{D}_\perp, \widehat{P})^\top$ in the variable $(\xi, k_\perp, t)$ which are derived from (B 4) may be recast as the system of temporal ODEs

$$\boldsymbol{M}_D \widehat{\boldsymbol{Z}}_D = \boldsymbol{M}_U\, \widehat{\boldsymbol{Z}}_U + \dot{\widehat{X}}_s\, \boldsymbol{S}^1 + \widehat{X}_s\, \boldsymbol{S}^0 + \widehat{\Phi}_{x\,D}\, \boldsymbol{E}_4, \tag{B 5}$$

with $\widehat{X}_s(k_\perp, t) \equiv \mathfrak{F}_{yz}[x_s^{(1)}(y, z, t)]$. In this formulation, $\boldsymbol{E}_4$ is the unit vector $(0, 0, 0, 1)^\top$, the matrices $\boldsymbol{M}_U$ and $\boldsymbol{M}_D$ are deduced from the expressions

$$\boldsymbol{M} = \begin{pmatrix} t^{\alpha-1} M_{11} & M_{12} & 0 & 0 \\ t^{2\alpha-2} M_{21} & t^{\alpha-1} M_{22} & 0 & -1 \\ 0 & 0 & 1 & 0 \\ t^{3\alpha-3} M_{41} & t^{2\alpha-2} M_{42} & 0 & t^{\alpha-1} M_{44} \end{pmatrix},$$

with

$$M_{11} = \bar{U}, \quad M_{12} = -\bar{G}, \quad M_{21} = \bar{U}\bar{V}, \quad M_{22} = \bar{G}(\bar{U} - \bar{V}), \quad M_{41} = \bar{U}\bar{V}^2/2,$$
$$M_{42} = \bar{G}\bar{V}\big(\bar{U} - \bar{V}/2\big) - \gamma\bar{P}/(\gamma - 1), \quad M_{44} = (\bar{W} - \gamma\bar{V})/(\gamma - 1),$$

while the vectors $\boldsymbol{S}^0$ and $\boldsymbol{S}^1$ read

$$\boldsymbol{S}^0 = -\begin{pmatrix} t^{-1}\bar{G}_D \mathrm{d}_\xi(\bar{G}\bar{U})|_D \\ t^{\alpha-2}\bar{G}_D \mathrm{d}_\xi(\bar{G}\bar{V}\bar{U} - \bar{P})|_D \\ t^{\alpha-1} k_\perp^2 [\bar{V}]_D^U \\ t^{2\alpha-3}\bar{G}_D \mathrm{d}_\xi\big[\big(\bar{P}/(\gamma - 1) + \bar{G}\bar{V}^2/2\big)\bar{U} - \bar{P}\bar{V} - \bar{\Phi}\big]|_D \end{pmatrix},$$

$$\boldsymbol{S}^1 = \begin{pmatrix} [\bar{G}]_D^U \\ t^{\alpha-1}[\bar{G}\bar{V}]_D^U \\ 0 \\ t^{2\alpha-2}[\bar{P}/(\gamma - 1) + \bar{G}\bar{V}^2/2]_D^U \end{pmatrix}.$$

B.2.2. *Reduced linear perturbation Rankine–Hugoniot relations*

The Rankine–Hugoniot jump relations for the linear perturbation reduced functions come readily from substituting (A 4), for both upstream and downstream flow quantities, into (B 4). Under the same assumption of a uniform upstream mean flow, we then obtain the equivalent of (B 5) under the form of the system of PDEs in the variable (η, ζ)

$$\boldsymbol{N}_D \mathscr{Z}_D - \mathscr{F}_{x\,D}\, \boldsymbol{E}_4 + \mathscr{X}_s\, \mathscr{S}^0 - \mathscr{W}\, \mathscr{S}^1 - \Delta_{(\eta,\zeta)} \mathscr{X}_s\, \mathscr{S}^2 = \boldsymbol{N}_U\, \mathscr{Z}_U, \tag{B 6}$$

with $\mathscr{Z} = (\mathscr{G}, \mathscr{V}_x, \nabla_{(\eta,\zeta)} \cdot \mathscr{V}_\perp, \mathscr{P})^\top$, and where

$$\mathscr{W} = [\delta(\beta - 1) + 1 - \beta\partial_\eta]\, \mathscr{X}_s,$$

represents the reduced shock-front deformation velocity whose expression is deduced from the boundary deformation relation (A 17). The matrices $\boldsymbol{N}_U$ and $\boldsymbol{N}_D$ follow from the definitions

$$\boldsymbol{N} = \begin{pmatrix} N_{11} & N_{12} & 0 & 0 \\ N_{21} & N_{22} & 0 & -1 \\ 0 & 0 & 1 & 0 \\ N_{41} & N_{42} & 0 & N_{44} \end{pmatrix},$$

with

$$N_{11} = \bar{\mathscr{U}}, \quad N_{12} = -\bar{\mathscr{G}}, \quad N_{21} = \bar{\mathscr{U}}\bar{\mathscr{V}}, \quad N_{22} = \bar{\mathscr{G}}(\bar{\mathscr{U}} - \bar{\mathscr{V}}), \quad N_{41} = \bar{\mathscr{U}}\bar{\mathscr{V}}^2/2,$$
$$N_{42} = \bar{\mathscr{G}}\bar{\mathscr{V}}(\bar{\mathscr{U}} - \bar{\mathscr{V}}/2) - \gamma\bar{\mathscr{P}}/(\gamma - 1), \quad N_{44} = (\bar{\mathscr{W}} - \gamma\bar{\mathscr{V}})/(\gamma - 1),$$

while the vectors $\mathscr{S}^0$, $\mathscr{S}^1$ and $\mathscr{S}^2$ are given by

$$\mathscr{S}^0 = \begin{pmatrix} \bar{\mathscr{G}}_D \mathrm{d}_\xi(\bar{\mathscr{G}}\bar{\mathscr{U}})|_D \\ \bar{\mathscr{G}}_D \mathrm{d}_\xi(\bar{\mathscr{G}}\bar{\mathscr{V}}\bar{\mathscr{U}} - \bar{\mathscr{P}})|_D \\ 0 \\ \bar{\mathscr{G}}_D \mathrm{d}_\xi[(\bar{\mathscr{P}}/(\gamma - 1) + \bar{\mathscr{G}}\bar{\mathscr{V}}^2/2)\bar{\mathscr{U}} - \bar{\mathscr{P}}\bar{\mathscr{V}} - \bar{\mathscr{F}}]|_D \end{pmatrix},$$

$$\mathscr{S}^1 = \begin{pmatrix} [\bar{\mathscr{G}}]_D^U \\ [\bar{\mathscr{G}}\bar{\mathscr{V}}]_D^U \\ 0 \\ [\bar{\mathscr{P}}/(\gamma - 1) + \bar{\mathscr{G}}\bar{\mathscr{V}}^2/2]_D^U \end{pmatrix}, \quad \mathscr{S}^2 = \begin{pmatrix} 0 \\ 0 \\ [\bar{\mathscr{V}}]_D^U \\ 0 \end{pmatrix}.$$

B.2.3. *Reduced Fourier mode Rankine–Hugoniot relations*

Considering the $\eta\zeta$-Fourier transform of (B 6) immediately yields the linear perturbation reduced Fourier mode jump relations, namely the system of ODEs in the wavenumber variable $\varkappa_\perp$

$$\boldsymbol{N}_D \widehat{\mathscr{Z}}_D - \widehat{\mathscr{F}}_{xD}\boldsymbol{E}_4 + \widehat{\mathscr{X}}_s(\mathscr{S}^0 - [\delta(\beta - 1) + 1]\mathscr{S}^1 + \varkappa_\perp^2 \mathscr{S}^2) - \beta\mathbb{D}\widehat{\mathscr{X}}_s \mathscr{S}^1 = \boldsymbol{N}_U \widehat{\mathscr{Z}}_U, \tag{B 7}$$

with the notation $\widehat{\mathscr{Z}} = (\widehat{\mathscr{G}}, \widehat{\mathscr{V}}_x, \widehat{\mathscr{D}}_\perp, \widehat{\mathscr{P}})^\top$, and where $\mathbb{D}$ is the operator introduced in (A 21).

REFERENCES

Abéguilé, F., Boudesocque-Dubois, C., Clarisse, J.-M., Gauthier, S. & Saillard, Y. 2006 Linear perturbation amplification in self-similar ablation flows of inertial confinement fusion. *Phys. Rev. Lett.* **97**, 035002.

Aglitskiy, Y., Velikovich, A. L., Karasik, M., Serlin, V., Pawley, C. J., Schmitt, A. J., Obenschain, S. P., Mostovych, A. N., Gardner, J. H. & Metzler, N. 2002 Direct observation of mass oscillations due to ablative Richtmyer–Meshkov instability and feedout in planar plastic targets. *Phys. Plasmas* **9**, 2264–2276.

Anisimov, S. I. 1970 Self-similar thermal wave in a two-temperature plasma heated by a laser pulse. *sov. phys. JETP Lett.* **12**, 287–289.

Barenblatt, G. 1979 *Similarity, Self-Similarity and Intermediate Asymptotics*. Consultants Bureau, New-York.

Barrero, A. & Sanmartín, J. R. 1977 Self-similar motion of laser fusion plasma. Absorption in an unbounded plasma. *Phys. Fluids* **20**, 1155–1163.

Betti, R., Goncharov, V. N., McCrory, R. L. & Verdon, C. P. 1995 Self-consistent cutoff wave number of the ablative Rayleigh–Taylor instability. *Phys. Plasmas* **2**, 3844–3851.

Betti, R., Goncharov, V. N., McCrory, R. L., Sorotokin, P. & Verdon, C. P. 1996 Self-consistent stability analysis of ablation fronts in inertial confinement fusion. *Phys. Plasmas* **3**, 2122–2128.

Bodner, S. E. 1974 Rayleigh–Taylor instability and laser-pellet fusion. *Phys. Rev. Lett.* **33**, 761–764.

Bodner, S. E., Colombant, D. G., Gardner, J. H., Lehmberg, R. H., Obenschain, S. P., Philipps, L., Schmitt, A. J., Sethian, J. D., McCrory, R. L., Seka, W., Verdon, C. P., Knauer, J. P., Afeyan, B. B. & Powell, H. T. 1998 Direct-drive laser fusion: status and prospects. *Phys. Plasmas* **5**, 1901–1918.

Boudesocque-Dubois, C. 2000 Perturbations linéaires d'une solution autosemblable de l'hydrodynamique avec conduction non linéaire. PhD thesis, Université de Paris 6.

Boudesocque-Dubois, C. & Clarisse, J.-M. 2003 Investigation of linear perturbation growth in a planar ablation flow. In *ECLIM 2002: 27th European Conference on Laser Interaction with Matter* (ed. O. N. Krokhin, S. Y. Gus'kov & Y. A. Merkul'ev), *Proc. SPIE*, vol. 5228, pp. 172–183.

Boudesocque-Dubois, C., Clarisse, J.-M. & Gauthier, S. 2001 Hydrodynamic stability of ablation fronts: linear perturbation of a self-similar solution. In *ECLIM 2000: 26th European Conference on Laser Interaction with Matter* (ed. M. Kálal, K. Rohlena & M. Šiňor), *Proc. SPIE*, vol. 4424, pp. 220–223.

Boudesocque-Dubois, C., Clarisse, J.-M. & Gauthier, S. 2003 A spectral Chebyshev method for linear stability analysis of one-dimensional exact solutions of gas dynamics. *J. Comput. Phys.* **184**, 592–618.

Boudesocque-Dubois, C., Gauthier, S. & Clarisse, J.-M. 2008 Self-similar solutions of unsteady ablation flows in inertial confinement fusion. *J. Fluid Mech.* **603**, 151–178.

Brueckner, K. A. & Jorna, S. 1974 Laser-driven fusion. *Rev. Mod. Phys.* **46**, 325–367.

Brun, L., Dautray, R., Delobeau, F., Patou, C., Perrot, F., Reisse, J.-M., Sitt, B. & Watteau, J.-P. 1977 Physical models and mathematical simulation of laser-driven implosion and their relations with experiments. In *Laser Interaction and Related Plasma Phenomena*, vol. 4B (ed. H. J. Schwarz & H. Hora), pp. 1059–1080. Plenum.

Buresi, E., Coutant, J., Dautray, R., Decroisette, M., Duborgel, B., Guillaneux, P., Launspach, J., Nelson, P., Patou, C., Reisse, J.-M. & Watteau, J.-P. 1986 Laser program development at CEL-V: overview of recent experimental results. *Laser Part. Beams* **4**, 531.

Bychkov, V. V., Golberg, S. M. & Liberman, M. A. 1991 Growth rate of the Rayleigh–Taylor instability in an ablatively accelerated inhomogeneous plasma. *Sov. Phys. JETP* **73**, 642–653.

Bychkov, V. V., Golberg, S. M. & Liberman, M. A. 1994 Self-consistent model of the Rayleigh–Taylor instability in ablatively accelerated laser plasma. *Phys. Plasmas* **1**, 2976–2986.

Clarisse, J.-M., Boudesocque-Dubois, C., Gauthier, S. & Abéguilé, F. 2006 Linear perturbation amplification in ICF self-similar ablation flows. *J. Phys. IV France* **133**, 111–115.

Duderstadt, J. & Moses, G. 1982 *Inertial Confinement Fusion*. Wiley-Interscience.

Emery, M. H., Gardner, J. H., Lehmberg, R. H. & Obenschain, S. P. 1991 Hydrodynamic target response to an induced spatial incoherence-smoothed laser beam. *Phys. Fluids* B **3**, 2640–2651.

Fortin, X. & Canaud, B. 2000 Direct drive laser fusion calculations at CEA. In *IFSA 99 — Inertial fusion sciences and applications* (ed. C. Labaune, W. J. Hogan & K. A. Tanaka), pp. 102–105. Elsevier.

Gauthier, S., Le Creurer, B., Abéguilé, F., Boudesocque-Dubois, C. & Clarisse, J.-M. 2005 A self-adaptive domain decomposition method with Chebyshev method. *Intl J. Pure Appl. Maths* **24**, 553–577.

Germain, P. & Muller, P. 1994 *Introduction à la mécanique des milieux continus*, 2nd edn. Masson, Paris.

Goncharov, V. N., Skupsky, S., Boehly, T. R., Knauer, J. P., McKenty, P., Smalyuk, V. A., Town, R. P., Gotchev, O. V., Betti, R. & Meyerhofer, D. D. 2000 A model of laser imprinting. *Phys. Plasmas* **7**, 2062–2068.

Goncharov, V. N., Gotchev, O. V., Vianello, E., Boehly, T. R., Knauer, J. P., McKenty, P. W., Radha, P. B., Regan, S. P., Sangster, T. C., Skupsky, S., Smalyuk, V. A., Betti, R., McCrory, R. L., Meyerhofer, D. D. & Cherfils-Clérouin, C. 2006 Early stage of implosion in inertial confinement fusion: shock timing and perturbation evolution. *Phys. Plasmas* **13**, 012702.

Gustafsson, B. & Sundström, A. 1978 Incompletely parabolic problems in fluid dynamics. *SIAM J. Appl. Maths* **35**, 343–357.

Holstein, P.-A., André, M., Casanova, M., Chaland, F., Charpin, C., Cherfils, C., Divol, L., Dumont, H., Galmiche, D., Giorla, J., Hallo, L., Laffite, S., Lours, L., Monteil, M.-C., Mourenas, D., Poggi, F., Saillard, Y., Schurtz, G., Valadon, M., Vanderhaegen, D. & Wagon, F. 2000 Target design for the LMJ. *CR Acad. Sci. Paris* **1**, ser. IV, 693–704.

Ishizaki, R. & Nishihara, K. 1997 Propagation of a rippled shock wave driven by nonuniform laser ablation. *Phys. Rev. Lett.* **78**, 1920–1923.

Kull, H. J. 1989 Incompressible description of Rayleigh–Taylor instabilities in laser-ablated plasmas. *Phys. Fluids* B **1**, 170–182.

Kull, H. J. & Anisimov, S. I. 1986 Ablative stabilization in the incompressible Rayleigh–Taylor instability. *Phys. Fluids* **29**, 2067–2075.

Landau, L. D. & Lifshitz, E. M. 1987 *Fluid Mechanics*. Pergamon.

Ledoux, P. & Walraven, T. 1958 Variable stars. In *Handbuch der Physik*, pp. 353–604. Springer.

Lombard, V., Boudesocque-Dubois, C., Clarisse, J.-M. & Gauthier, S. 2007 Kovàsznay modes in stability of self-similar ablation flows. In *34th EPS Conference on Plasma Physics*, *Europhysics Conference Abstracts*, vol. 31F. EPS.

Marshak, R. 1958 Effect of radiation on shock wave behavior. *Phys. Fluids* **1**, 24–29.

Meshkov, E. E. 1969 Instability of the interface of two gases accelerated by a shock wave. *Sov. Fluid Dyn.* **4**, 101–104.

Metzler, N., Velikovich, A. L. & Gardner, J. H. 1999 Reduction of early-time perturbation growth in ablatively driven laser target using tailored density profiles. *Phys. Plasmas* **6**, 3283–3295.

Metzler, N., Velikovich, A. L., Schmitt, A. J., Karasik, M., Serlin, V., Mostovych, A. N., Obenschain, S. P., Gardner, J. H. & Aglitskiy, Y. 2003 Laser imprint reduction with a shaping pulse, oscillatory Richtmyer–Meshkov to Rayleigh–Taylor transition and other coherent effects in plastic-foam targets. *Phys. Plasmas* **10**, 1897–1905.

Nishihara, K., Ishizaki, R., Wouchuk, J. G., Fukuda, Y. & Shimuta, Y. 1998 Hydrodynamic perturbation growth in start-up phase in laser implosion. *Phys. Plasmas* **5**, 1945–1952.

Nuckolls, J., Wood, L., Thiessen, A. & Zimmerman, G. 1972 Laser compression of matter to super-high densities: thermonuclear (CTR) applications. *Nature* **239**, 139–142.

Pakula, R. & Sigel, R. 1985 Self-similar expansion of dense matter due to heat transfer by nonlinear conduction. *Phys. Fluids* **28**, 232–244.

Piriz, A. R. 2001*a* Hydrodynamic instability of ablation fronts in inertial confinement fusion. *Phys. Plasmas* **8**, 997–1002.

Piriz, A. R. 2001*b* Compressibility effects on the Rayleigh–Taylor instability of an ablation front. *Phys. Plasmas* **8**, 5268–5276.

Piriz, A. R. & Portugues, R. F. 2003 Landau–Darrieus instability in an ablation front. *Phys. Plasmas* **10**, 2449–2456.

Piriz, A. R., Sanz, J. & Ibañez, L. F. 1997 Rayleigh–Taylor instability of steady ablation fronts: the discontinuity model revisited. *Phys. Plasmas* **4**, 1117–1126.

Pulicani, J. P. 1988 A spectral multi-domain method for the solution of 1-D-Helmholtz and Stokes-type equations. *Computers Fluids* **16**, 207–215.

Rayleigh, Lord 1883 Investigation of the character of the equilibrium of an incompressible heavy fluid of variable density. *Proc. Lond. Math. Soc.* **14**, 170–177 (In *Scientific Papers*, vol. 2, pp. 200–207. Cambridge University Press 1900.)

Reinicke, P. & Meyer-ter-Vehn, J. 1991 The point explosion with heat conduction. *Phys. Fluids* A **3**, 1807–1818.

Richtmyer, R. D. 1960 Taylor instability in shock acceleration of compressible fluids. *Commun. Pure Appl. Maths* **13**, 297–319.

Sanmartín, J. R. & Barrero, A. 1978*a* Self-similar motion of laser half-space plasma. I. Deflagration regime. *Phys. Fluids* **21**, 1957–1966.

Sanmartín, J. R. & Barrero, A. 1978*b* Self-similar motion of laser half-space plasma. II. Thermal wave and intermediate regimes. *Phys. Fluids* **21**, 1967–1971.

Sanz, J. 1996 Self-consistent analytical model of the Rayleigh–Taylor instability in inertial confinement fusion. *Phys. Rev.* E **53**, 4026–4045.

Sanz, J., Piriz, A. R. & Tomasel, F. G. 1992 Self-similar model for tamped ablation driven by thermal radiation. *Phys. Fluids* B **4**, 683–692.

Sanz, J., Masse, L. & Clavin, P. 2006 The linear Darrieus–Landau and Rayleigh–Taylor instabilities in inertial confinement fusion revisited. *Phys. Plasmas* **13**, 102702.

Schmitt, A. J., Velikovich, A. L., Gardner, J. H., Pawley, C., Obenschain, S. P., Aglitskiy, Y. & Chan, Y. 2001 Growth of pellet imperfections and laser imprint in direct drive inertial confinement fusion targets. *Phys. Plasmas* **8**, 2287–2295.

Stoker, J. J. 1958 *Water Waves*. Wiley-Interscience.

Strikwerda, J. C. 1977 Initial boundary value problems for incompletely parabolic systems. *Commun. Pure Appl. Maths* **30**, 797–822.

Takabe, H., Mima, K., Montierth, L. & Morse, R. L. 1985 Self-consistent growth rate of the Rayleigh–Taylor instability in an ablatively accelerating plasma. *Phys. Fluids* **28**, 3676–3682.

Taylor, G. I. 1950 The instability of liquid surfaces when accelerated in a direction perpendicular to their planes. I. *Proc. R. Soc. Lond.* A **201**, 192–196.

Taylor, R. J., Dahlburg, J. P., Iwase, A., Gardner, J. H., Fyfe, D. E. & Willi, O. 1996 Measurement and simulation of laser imprinting and consequent Rayleigh–Taylor growth. *Phys. Rev. Lett.* **76**, 1643–1646.

Velikovich, A. L., Dahlburg, J. P., Gardner, J. H. & Taylor, R. J. 1998 Saturation of perturbation growth in ablatively driven planar laser targets. *Phys. Plasmas* **5**, 1491–1505.

Williamson, J. H. 1980 Low-storage Runge–Kutta schemes. *J. Comput. Phys.* **35**, 48–56.

Zel'dovich, Y. & Raizer, Y. 1967 *Physics of Shock Waves and High-Temperature Hydrodynamic Phenomena*. Academic.